

# Exact muffin-tin orbital based fully relativistic simulation of device materials: Electronic charge and spin current

Zhiyi Chen,<sup>1,2,4,\*</sup> Qingyun Zhang ,<sup>1,\*</sup> Yu Zhang,<sup>1</sup> Lei Wang ,<sup>3</sup> Mankun Sang,<sup>1</sup> and Youqi Ke<sup>1,2,4,†</sup>

<sup>1</sup>*School of Physical Science and Technology, ShanghaiTech University, Shanghai 201210, China*

<sup>2</sup>*Shanghai Institute of Optics and Fine Mechanics, Chinese Academy of Sciences, Shanghai 201800, China*

<sup>3</sup>*State Key Laboratory for Mechanical Behavior of Materials, Center for Spintronics and Quantum Systems, Xi'an Jiaotong University, No. 28 Xianning West Road Xi'an, Shaanxi 710049, China*

<sup>4</sup>*University of Chinese Academy of Sciences, Beijing 100049, China*



(Received 13 April 2020; revised 28 May 2020; accepted 16 June 2020; published 2 July 2020)

We report the implementation of the fully relativistic exact muffin-tin orbital (EMTO) method for both first-principles electronic structure and quantum transport simulation of magnetic and nonmagnetic device materials. We consider a device-material system containing the inevitable atomic disorders in contact with different electrode materials. The Kohn-Sham Dirac equations for both cases with and without spin polarization are self-consistently solved for the central device-material system with the Green's function method. The fully relativistic charge-current density, conventional Pauli spin current density, and transmission coefficient are formulated with the nonequilibrium Green's function technique. To treat the influence of disordered defects/impurities, we combine the nonequilibrium Green's function in the Keldysh space with the coherent potential approximation, and account for the multiple disorder scattering by vertex corrections to a two-Green's-function correlator to calculate the disorder-averaged charge and spin current density. As a demonstration of the present implementation, we calculate the electronic structure of the bulk Pt, Co, and HgTe and Rashba-type surface states of Au and Ag/Ag<sub>2</sub>Bi<sub>1</sub> alloy surfaces. We find that the EMTO electronic structures of all the calculated systems agree well with the results of the projector-augmented wave method. The electronic charge and spin transport implementations are tested with perfect and disordered Cu/Co/Pt/Cu junctions. The important effects of interface and atomic disorders are illustrated for the spin transport in the presence of relativistic effects. The implementation of the fully relativistic EMTO-based device-material simulation provides an important tool for analyzing both the charge and spin transport through nanostructures and materials, significantly extending the capability of first-principles material design for spintronic device applications.

DOI: [10.1103/PhysRevB.102.035405](https://doi.org/10.1103/PhysRevB.102.035405)

## I. INTRODUCTION

The relativistic effect is essential for numerous physical properties of materials and devices [1,2]. Especially, as an important relativistic effect, the spin-orbit interaction (SOI), originating from electrons' movement in the intrinsic electric field of materials, gives rise to many important phenomena of quantum materials and spintronic device applications, including magnetocrystalline anisotropy [3,4], spin-orbit torque [5], the spin Hall effect [5], the anomalous Hall effect [6], topological materials [7,8], and spin field-effect transistors [9]. Developing first-principles relativistic device-level material simulation is thus important for understanding the role of different materials, interfaces, and disordered defects on the relativistic effect based phenomena and device functionalities. Presently, in most implementations of Kohn-Sham density functional theory (KSDFT) [10,11] based first-principles methods, the SOI is included, to account for the relativistic effect, as a perturbation in the nonrelativistic limit, for example in the

Vienna *ab initio* simulation package (VASP) [12], Siesta package [13], the full potential linearized muffin-tin orbital method (LMTO) [14], and linearized augmented plane wave method [15]. However, this type of perturbation approach has found difficulties for effectively treating atomic disorders and for the elements with orbital moment comparable to the spin moment. The fully relativistic implementation of DFT can be realized by directly solving the Kohn-Sham Dirac equation, for example, the KKR [16], LMTO in the atomic sphere approximation [17], and exact muffin-tin orbital (EMTO) [18] methods. However, most of the implementations are only for bulk-type materials simulation, not for quantum transport calculation of device materials that features the nonequilibrium, open-boundary conditions and large system size.

The EMTO method, as the third generation of MTO first proposed by Andersen and coworkers [19–22], is highly accurate and efficient for first-principles materials simulation. EMTO features the localized, minimal, and complete basis set, possessing great potential for solving challenges in device-materials simulation. Vitos *et al.* and Purovskii *et al.* made the first successful implementation of the respective scalar relativistic (SR) EMTO [23–25] and fully relativistic (FR) EMTO [18] for first-principles bulk-materials

\*These two authors contributed equally to this work.

†keyq@shanghaitech.edu.cn

simulation. It has been demonstrated that the results of the first-principles EMTO method present very good agreement with the all-electron full-potential linear augmented wave method for different bulk systems [23]. Very recently, some of the authors have reported the successful implementation of the SR-EMTO method for quantum transport simulation of device-level materials and showed that the EMTO results agree very well with the projector-augmented wave method and experimental measurements for device materials [26].

In this work, we report our implementation of the FR-EMTO method for fully relativistic first-principles simulation of electron and spin transport through magnetic and nonmagnetic device materials, as an important extension of the capability of EMTO-based first-principles device simulation. We combine the FR-EMTO method with the Keldysh nonequilibrium Green's function (NEGF) technique to formulate the electronic charge and spin transport properties for a device in contact with different electrodes. To treat the disorder scattering, the coherent potential approximation (CPA) is combined with the NEGF method and the nonequilibrium vertex correction is included to calculate the disorder-averaged charge and spin current. As a demonstration of FR-EMTO for device-materials simulation, we calculate the electronic structure of bulk Co, Pt, and HgTe and Rashba-type surface states for Au and Ag/Ag<sub>2</sub>Bi<sub>1</sub> surfaces and the charge and spin transport through the perfect and disordered Cu/Co/Pt/Cu junctions, and compare our results with the PAW and SR-EMTO calculations and experimental measurements.

The rest of the paper is organized as follows: Section II provides a brief review of the basic formalism of the FR-EMTO method. Section III presents the NEGF method in Keldysh space with the FR-EMTO method for the electronic structure and quantum transport calculation; in Sec. IV, the coherent potential approximation is combined with the Keldysh NEGF to do the disorder average, accounting for multiple scattering by disordered defects inevitable in realistic devices; in Sec. V, we derive the relativistic electron charge current and Pauli spin current formula with the NEGF technique for both ordered and disordered devices. In Sec. VI, we present some information about the self-consistent implementation and numerical results. Finally, we conclude our work in Sec. VII and provide more information in Appendices A, B, C, and D.

## II. FULLY RELATIVISTIC EXACT MUFFIN-TIN ORBITAL METHOD

We consider the Kohn-Sham Dirac equation for a magnetic system,

$$\hat{H} = c\vec{\alpha} \cdot \vec{p} + (\beta - I_4)mc^2 + V(\vec{r}) + \beta\vec{\Sigma} \cdot \vec{B}(\vec{r}) \quad (1)$$

and

$$\vec{\alpha} = \begin{pmatrix} 0 & \vec{\sigma} \\ \vec{\sigma} & 0 \end{pmatrix}, \quad \beta = \begin{pmatrix} I_2 & 0 \\ 0 & -I_2 \end{pmatrix}, \quad \vec{\Sigma} = \begin{pmatrix} \vec{\sigma} & 0 \\ 0 & \vec{\sigma} \end{pmatrix}, \quad (2)$$

where  $\sigma$  is the Pauli matrix. In the muffin-tin approximation, the effective full potential is approximated as

$$V(\vec{r}) \approx V_{mt}(\vec{r}) \equiv V_{mz} + \sum_R [V_R(r_R) - V_{mz}], \quad (3)$$

and the magnetic field is approximated as

$$\vec{B}(\vec{r}) \approx \vec{B}_{mt}(\vec{r}) \equiv \sum_R \vec{B}_R(r_R), \quad (4)$$

where  $V_R(r_R)$  is a spherical potential centered on lattice site  $R$  and  $V_{mz}$  is a constant potential (we use the notation  $\vec{r}_R = \vec{r} - \vec{R}$ , and  $r_R = |\vec{r}_R|$ ). We can solve the single-electron Dirac equation with the muffin-tin potential, by expanding the Kohn-Sham orbital in terms of EMTO as

$$\Psi_j(\vec{r}) = \sum_{R\Lambda} \Phi_{R\Lambda}^a(\epsilon_j, \vec{r}_R) \psi_{R\Lambda, j}^a. \quad (5)$$

Here the EMTO, as an important first-principles method, allows large overlapping potential spheres that provide a more accurate description of the potential compared to the conventional approximation. Moreover, the EMTO method treats the interstitial and atomic regions on the same footing, and thus can provide important accuracy for simulating disordered systems and interfaces/surfaces of various materials. Here, we provide a brief introduction to the FR-EMTO for solving the Dirac equation (1) with spin polarization. (For more information about FR-EMTO, please refer to Ref. [18] implemented for bulk materials, and Ref. [27].)

The energy-dependent smooth FR-EMTO is composed of three parts as follows:

$$\Phi_{R\Lambda}^a(\epsilon, \vec{r}_R) = \phi_{R\Lambda}^a - \varphi_{R\Lambda}^a + \psi_{R\Lambda}^a, \quad (6)$$

including the four-component partial wave  $\phi_{R\Lambda}^a$ , free electron solution  $\varphi_{R\Lambda}^a$ , and the screened spherical wave (SSW)  $\psi_{R\Lambda}^a$ , where the relativistic quantum number  $\Lambda = \kappa\mu$ . Here, the superscript  $a$  denotes the screening representation. The partial wave  $\phi_{R\Lambda}^a$  is defined inside each overlapping potential sphere ( $s_R$ ) as [27]

$$\phi_{R\Lambda}^a(E, \vec{r}_R) = \sum_{\lambda=\kappa, -\kappa-1} \phi_{R\lambda\mu}^a N_{R,\lambda\kappa}^{a,\mu}, \quad (7)$$

where  $\phi_{R\lambda\mu}^a$  is solved from the coupled radial Dirac equation for a general magnetic system and  $N_{R,\lambda\kappa}^{a,\mu}$  is the normalization matrix. The SSW  $\psi_{R\Lambda}^a$  with pure spin-spherical wave, serving as the envelope function, satisfies the interstitial Dirac equation with constant potential, and can be generally expanded around other sites  $R'$  as [16,18]

$$\psi_{R\Lambda}^a(\kappa^2, \vec{r}_R) = f_{R\Lambda}^a(\kappa^2, \vec{r}_R) \delta_{RR'} - \sum_{R'\Lambda'} g_{R'\Lambda'}^a(\kappa^2, \vec{r}_{R'}) S_{R'\Lambda', R\Lambda}^a(\kappa^2), \quad (8)$$

where  $f_{R\Lambda}^a$  and  $g_{R\Lambda}^a$  are the respective head and tail functions and  $S^a$  is the screened slope matrix which is obtained by the general screening technique of the Methfessel formulation [28] (namely, by imposing proper boundary conditions on a set of nonoverlapping screening spheres of radius  $a_R$  so that it equals pure spin-spherical harmonic waves on its own  $a$  sphere and vanishes on and inside other  $a$  spheres) [19–25]. It has been shown that by carefully choosing boundary conditions on the screening spheres  $a_R$ , the fully relativistic  $S_{R'\Lambda', R\Lambda}^a(\kappa^2)$  can be connected to the nonrelativistic  $S_{R'L', RL}^a$  by

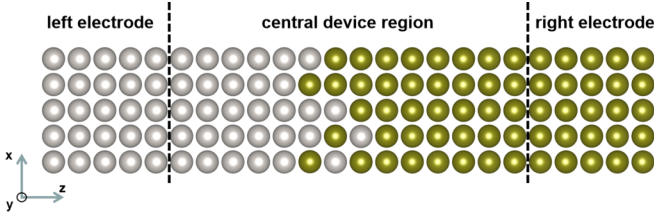


FIG. 1. Schematic illustration of two-probe device containing a central device region contacting the left and right electrodes.

[18]

$$S_{R'L',RL}^a(k^2) = \sum_{s=\pm 1/2} c\left(l'j'\frac{1}{2}; \mu' - s, s\right) \times S_{R'L,RL}^a(k^2) c\left(lj\frac{1}{2}; \mu - s, s\right), \quad (9)$$

where  $c(lj\frac{1}{2}; \mu - s, s)$  is the Clebsch-Gordan coefficient, providing an important basis for developing FR-EMTO first-principles methods from the implementation of SR-EMTO. To make the FR-EMTO smooth, the free electron solution  $\varphi_{R\Lambda}^a$  is introduced in the region between the screening and potential spheres so that FR-EMTO is continuous at both  $a_R$  and  $s_R$ , and differentiable at  $s_R$  [19–25],

$$\varphi_{R\Lambda}^a = f_{R\Lambda}^a - \sum_{\lambda=\kappa, -\kappa-1} g_{R\lambda\mu}^a D_{R,\lambda\kappa}^{a,\mu}, \quad (10)$$

where the matrix elements of  $D_R^a(\epsilon)$  are obtained by satisfying the boundary conditions.

Similarly to the SR-EMTO, the overlap matrix of the FR-EMTO, namely  $\langle \Phi^a | \Phi^a \rangle$ , can be approximated in the threefold way as [19–22]

$$O = \langle \Phi^a | \Phi^a \rangle = \langle \phi^a | \phi^a \rangle - \langle \varphi^a | \varphi^a \rangle + \langle \psi^a | \psi^a \rangle = -a\dot{D}^a(\epsilon) + a\dot{S}^a(\epsilon) = \dot{K}^a(\epsilon). \quad (11)$$

Here  $K = aS^a - aD^a$  is called the kink matrix. Moreover, the FR-EMTO matrix  $\langle \Phi^a | \epsilon - \hat{H} | \Phi^a \rangle$  in the threefold approximation can be obtained as [19–22]

$$\langle \Phi^a | \epsilon - \hat{H} | \Phi^a \rangle = aS^a(\epsilon) - aD^a(\epsilon) = K^a(\epsilon). \quad (12)$$

It is clear that the  $K^a$  is as short-ranged as the screened slope matrix  $S^a$ , providing the high efficiency for the computation with EMTO.

### III. FR-EMTO-BASED KELDYSH NEGF METHOD FOR DEVICE MATERIALS

As shown in Fig. 1, we consider a specific device-material system, containing a central device region sandwiched by different semi-infinite electrodes. In the operating state, the current flows through the central device region, making the device at the nonequilibrium state. As is known, the most rigorous theoretical framework for treating the nonequilibrium quantum transport problem is the nonequilibrium Green's function (NEGF) theory. The NEGF theory provides a general solution to the complex nonequilibrium problem with

various scattering mechanisms including electron-phonon and random impurity scattering [29–35]. Here, we introduce the key ideas of the NEGF theory to combine with the FR-EMTO method for realizing the first-principles fully relativistic quantum transport simulation.

In the Keldysh NEGF theory, the central quantity is the contour-ordered Green's function defined on the Keldysh closed time contour,

$$\mathbf{G}(\vec{r}, t; \vec{r}', t') = -i \langle \Phi | T_c [\psi_{\mathcal{H}}(\vec{r}, t) \psi_{\mathcal{H}}^\dagger(\vec{r}', t')] | \Phi \rangle, \quad (13)$$

where  $T_c$  denotes the contour-ordered operator, and  $\psi_{\mathcal{H}}$  and  $\psi_{\mathcal{H}}^\dagger$  are the respective elimination and creation field operators defined in the Heisenberg picture. (Note that in the rest of the paper, we use the bold font to denote the contour-ordered quantities.) In the above equation, the time evolution starts from the remote past, passes through  $t$  and  $t'$ , and finally returns to the remote past again. Importantly, the contour-ordered GF in Eq. (13) features the same mathematical structure as the time-ordered equilibrium GF defined on the real-time axis  $-\infty \rightarrow +\infty$  [30]. The contour-ordered GF thus satisfies the Dyson equation in a compact form, providing the basis for general applications,

$$\mathbf{G} = \mathbf{G}_0 + \mathbf{G}_0 \mathbf{\Sigma} \mathbf{G}, \quad (14)$$

with the self-energy  $\mathbf{\Sigma}$  accounting for the effects of complex interactions and  $\mathbf{G}_0$  denoting the GF of unperturbed  $H_0$ . It should be emphasized that the contour-ordered GF not only directly relates to physical observables, but also makes the complex nonequilibrium quantum problem tractable. For practical applications, we introduce the Keldysh rotation technique [36], namely the  $2 \times 2$  Keldysh real-time matrix representation of the contour-ordered quantity, as an alternative to the analytical continuation method (Langreth theorem) [29],

$$\mathbf{G} = \begin{pmatrix} G^A & 0 \\ G^K & G^R \end{pmatrix}, \quad (15)$$

where  $G^{R/A}$  are the retarded and advanced GFs, and  $G^K$  is the Keldysh GF. With the GFs  $G^{R/A/K}$ , other real-time GFs or Craig representation [37] can be obtained by their linear combination or simple unitary transformation [38], such as the lesser GF  $G^< = \frac{1}{2}(G^K + G^A - G^R)$ .

For the device in Fig. 1, only the GFs or properties of the central device region are of interest, while the left and right electrodes, serving as the reservoirs, are assumed in equilibrium state, and can be treated with bulk calculations separately. As a direct application of the NEGF theory, the contour-ordered GF of the central device  $\mathbf{G}_{CC}$  can be straightforwardly obtained by treating the electrodes with the self-energies, namely

$$\mathbf{G}_{CC} = \mathbf{G}_{CC,0} + \mathbf{G}_{CC,0} \mathbf{\Sigma}_{ld} \mathbf{G}_{CC}, \quad (16)$$

where  $\mathbf{G}_{CC,0}$  is the GF of the isolated central part and the electrode self-energy  $\mathbf{\Sigma}_{ld} = \mathbf{\Sigma}_{ld,L} + \mathbf{\Sigma}_{ld,R}$  describes the coupling of the semi-infinite left/right electrode to the central region. Within the Keldysh representation, in the FR-EMTO method,  $\mathbf{G}_{CC}$  can be rewritten as (after transforming to the energy

domain)

$$\mathbf{G}_{CC} = (\mathbf{K}_{CC} - \Sigma_{ld})^{-1}, \quad (17)$$

where

$$\mathbf{K}_{CC} = \begin{pmatrix} K_{CC}^{\mathcal{K}} & 0 \\ K_{CC}^{\mathcal{R}} & K_{CC}^{\mathcal{A}} \end{pmatrix}, \quad \Sigma_{ld} = \begin{pmatrix} \Sigma_{ld}^{\mathcal{A}} & 0 \\ \Sigma_{ld}^{\mathcal{K}} & \Sigma_{ld}^{\mathcal{R}} \end{pmatrix}. \quad (18)$$

Here  $K_{CC}^{\mathcal{R}/\mathcal{A}} = K_{CC}^{\pm}$  and  $K_{CC}^{\mathcal{K}} = 0$  due to the Hermitian kink matrix;  $\Sigma_{ld}^{\mathcal{K}} = (2f_L - 1)(\Sigma_{ld,L}^{\mathcal{A}} - \Sigma_{ld,L}^{\mathcal{R}}) + (2f_R - 1)(\Sigma_{ld,R}^{\mathcal{A}} - \Sigma_{ld,R}^{\mathcal{R}})$  due to the fact that semi-infinite electrodes are in the equilibrium state ( $f_{L/R}$  are the Fermi function of electrodes). Finally, with Eqs. (17) and (18), we can explicitly write, for each component,

$$G_{CC}^{\mathcal{R}/\mathcal{A}} = (K_{CC} - \Sigma_{ld}^{\mathcal{R}/\mathcal{A}})^{-1}, \quad (19a)$$

$$G_{CC}^{\mathcal{K}} = G_{CC}^{\mathcal{R}} \Sigma_{ld}^{\mathcal{K}} G_{CC}^{\mathcal{A}}. \quad (19b)$$

With the GFs  $G_{CC}^{\mathcal{R}/\mathcal{A}/\mathcal{K}}$ , the device physical properties, including charge density, charge current, and Pauli spin current, can be calculated with FR-EMTO.

It should be mentioned that for solving the device at equilibrium, one only needs to compute Eq. (19a) and use the fluctuation dissipation theorem, namely  $G^< = (G^{\mathcal{A}} - G^{\mathcal{R}})$  ( $G^{\mathcal{A}} = G^{\mathcal{R},+}$ ), to calculate the equilibrium electronic structure of the device materials. One can also check the fact that, with Eq. (19b), the lesser  $G^<$  restores the fluctuation-dissipation theorem to equilibrium, which is the basis for equilibrium calculation. In our implementation, we divide the two-probe device system into principal layers along the transport direction (which is large enough so that the kink matrix become tridiagonal) and apply the recursive Green's function technique [26,39]. For other information for computing the Green's function of the central device region, such as the computation of electrode self-energies and on-layer and off-layer blocks of GFs, please refer to the previous implementation of SR-EMTO for device materials in Ref. [26].

#### IV. COHERENT POTENTIAL APPROXIMATION IN KELDYSH SPACE FOR EMTO METHOD

Here we consider the realistic system containing substitutional disorders, namely  $A_x B_{1-x}$ , with different chemical occupants on the underlying lattice. For such disordered system, the kink matrix elements in EMTO can be written as, for a specific disorder configuration,

$$K_{R,R'}^a = - \sum_Q \eta_R^Q a_R D_R^{a,Q} \delta_{R,R'} + a_R S_{R,R'}^a, \quad (20)$$

where the occupation operator  $\eta_R^Q = 1$  if a  $Q$  atom is at the  $R$  site, and  $\eta_R^Q = 0$  otherwise. The disordered quantity is  $D_R^Q$  due to the randomly distributed atom  $Q$ , and the slope matrix is independent of disorder, presenting a site-diagonal disorder problem in the FR-EMTO method. As an important result, the well-established conventional coherent potential approximation (CPA) [40,41] can be combined with the EMTO method to do the disorder average from first principles [18,42]. The CPA obtains the averaged GF of a disordered system by self-consistently constructing an effective medium with translational invariance. Presently, with the EMTO method, CPA has

been first implemented by Vitos *et al.* with important applications for bulk materials [25,42–47] and by some of the authors for quantum transport simulation of device materials [26]. Here, we present the generalized CPA in Keldysh space within the FR-EMTO method for first-principles fully relativistic quantum transport simulation of device materials. Differently from previous implementations, we here consider the disorder average of the contour-ordered GF for a disordered device material system at nonequilibrium.

To simplify the situation, we only consider the disorders inside the central device region; namely the electrode self-energies in Eq. (19) are independent of the disorders. To describe the averaged contour-ordered GF, we can introduce an effective Keldysh  $\mathcal{D}_R^a$  function in  $2 \times 2$  matrix form for all the disordered sites

$$\mathcal{D}_R^a = \begin{pmatrix} \mathcal{D}_R^{a,\mathcal{A}} & 0 \\ \mathcal{D}_R^{a,\mathcal{K}} & \mathcal{D}_R^{a,\mathcal{R}} \end{pmatrix}, \quad \mathcal{D}^a = \sum_R \mathcal{D}_R^a \quad (21)$$

(note that  $\mathcal{D}_R^{a,\mathcal{K}} \neq 0$ ). Therefore, we have the averaged contour-ordered GF, for the central device,

$$\mathcal{G}_{CC}^a = \{a_C [S_{CC}^a - \mathcal{D}_C^a] - \Sigma_{ld}^a\}^{-1}. \quad (22)$$

As a result, by applying the Dyson equation, namely Eq. (14), the Green's function  $G_{CC}^a$  of a specific disorder configuration can be expressed as  $G_{CC}^a = \mathcal{G}_{CC}^a + \mathcal{G}_{CC}^a T_{CC} \mathcal{G}_{CC}^a$  by defining  $T_{CC} = \Delta(1 - \mathcal{G}_{CC}^a \Delta)^{-1}$  with  $\Delta_R = a_{Rl}[-\mathcal{D}_R^a + \mathcal{D}_R^a]$ . (Note that the Keldysh matrix features a lower triangular matrix; the matrix addition, multiplication, and inverse operations on Keldysh matrices do not change the mathematical structure.) Here the Keldysh matrix  $T = \begin{pmatrix} T^{\mathcal{A}} & 0 \\ T^{\mathcal{K}} & T^{\mathcal{R}} \end{pmatrix}$  accounts for the total effect of disorders at nonequilibrium. Then, by taking the disorder average to  $\mathcal{G}_{CC}^a$ , the CPA self-consistent condition  $\langle T_{CC} \rangle = 0$  is obtained to solve for the effective medium  $\mathcal{D}_C^a$ . To make CPA practical, according to the conventional CPA, the single-site approximation (SSA) is usually introduced to reduce the CPA condition to a single-site equation [38,40,41],

$$\langle t_R \rangle = \sum_Q c_R^Q t_R^Q = 0, \quad (23)$$

where the single-site scatter in Keldysh space is defined as  $t_R = \Delta_R(1 - \mathcal{G}^a \Delta_R)^{-1}$ . According to the definition of the Keldysh matrix, we can find

$$t_R^{\mathcal{R}/\mathcal{A},Q} = \Delta_R^{\mathcal{R}/\mathcal{A}}(1 - \mathcal{G}^{\mathcal{R}/\mathcal{A}} \Delta_R^{\mathcal{R}/\mathcal{A}})^{-1}, \\ t_R^{\mathcal{K},Q} = t_R^{\mathcal{R},Q} \mathcal{G}^{\mathcal{K}} t_R^{\mathcal{A},Q} - (1 + t_R^{\mathcal{R},Q} \mathcal{G}^{\mathcal{R}}) \mathcal{D}_R^{\mathcal{K}} (1 + \mathcal{G}^{\mathcal{A}} t_R^{\mathcal{A},Q}).$$

With the SSA, the single-site effective quantities  $\mathcal{D}_R^{a,\mathcal{R}/\mathcal{A}/\mathcal{K}}$  for each site can be efficiently solved to obtain the total coherent medium by  $\mathcal{D}^a = \sum_R \mathcal{D}_R^a$ . The SSA neglects all nonlocal correlation of disorder scattering and local environment effects, presenting the major limitation for the CPA. However, we note that the recent development of the dynamical cluster approximation and the dual-fermion technique can provide an effective way to include some nonlocal corrections and treat the effects of short-range order of disorders [48,49].

After the CPA self-consistency is achieved, we obtain the averaged GF  $\mathcal{G}$ . Moreover, in many applications, conditionally averaged GFs, namely  $\mathcal{G}_{RR}^Q$  and  $\mathcal{G}_{RR'}^{QQ'}$ , are required, for

example, the electronic structure self-consistency and many physical properties including the charge and spin current density (see Sec. V). The conditionally averaged contour-ordered GF can be defined with the occupation operator as follows:

$$\begin{aligned} \mathcal{G}_{RR}^Q &= \frac{1}{c_R^Q} \langle \eta_R^Q \mathbf{G} \rangle_{RR}, \\ \mathcal{G}_{RR'}^{QQ'} &= \frac{1}{c_R^Q c_{R'}^{Q'}} \langle \eta_R^Q \mathbf{G} \eta_{R'}^{Q'} \rangle_{RR'}, \quad (R \neq R'). \end{aligned} \quad (24)$$

As shown in Appendix A with SSA, the quantities  $\mathcal{G}_{RR}^Q$  and  $\mathcal{G}_{RR'}^{QQ'}$  can be obtained by

$$\begin{aligned} \mathcal{G}_{RR}^Q &= (\mathcal{G} + \mathcal{G} t_R^Q \mathcal{G})_{RR}, \\ \mathcal{G}_{RR'}^{QQ'} &= [(1 + \mathcal{G} t_R^Q \mathcal{G} (1 + t_{R'}^{Q'} \mathcal{G}))]_{RR'}. \end{aligned} \quad (25)$$

With the above relations, one can explicitly obtain the GFs  $\mathcal{G}_{RR}^{R/A/K,Q}$  in Eq. (A10) and  $\mathcal{G}_{RR'}^{R/A/K,QQ'}$  in Eq. (A11), and finally all the real-time GFs can be thus obtained, such as the lesser GF,

$$\mathcal{G}_{RR'}^{<,Q/QQ'} = \frac{1}{2} (\mathcal{G}_{RR'}^{A,Q/QQ'} - \mathcal{G}_{RR'}^{R,Q/QQ'} + \mathcal{G}_{RR'}^{K,Q/QQ'}). \quad (26)$$

## V. NEGF-BASED FULLY RELATIVISTIC QUANTUM TRANSPORT

In the following, we introduce the formalism of the electron charge and Pauli-spin transport with the FR-EMTO method in combination with the NEGF technique for the fully relativistic quantum transport simulation.

### A. Electron charge transport and transmission coefficient

As known, the charge current directly describes the time variance of charge, namely  $e \frac{d}{dt} (\Psi^\dagger \Psi)$ . As shown in Appendix B,  $e \frac{d}{dt} (\Psi^\dagger \Psi) = -\nabla \cdot \vec{J}(\vec{r})$ , namely the continuity equation, where the fully relativistic electron-charge current density can be given by  $\vec{J}(\vec{r}) = e [c \Psi^\dagger(\vec{r}) \vec{\alpha} \Psi(\vec{r})] = ec \text{Tr}[\vec{\alpha} \Psi(\vec{r}') \Psi^\dagger(\vec{r})]_{\vec{r}=\vec{r}'}$ . Here  $c\vec{\alpha} = \frac{i}{\hbar} [\hat{H}, \vec{r}]$  is the velocity operator in FR quantum mechanics, and the charge is conserved and relativistically invariant. With the NEGF method, the real-space electron-charge current density can be calculated as (in the energy domain)

$$\begin{aligned} J(E, \vec{r}) &= ec \text{Tr}[\vec{\alpha} G^<(E, \vec{r}, \vec{r}')]_{\vec{r}=\vec{r}'} \\ &= ec \text{Tr} \left[ \sum_{R\Lambda, R'\Lambda'} G_{R'\Lambda', R\Lambda}^< \Phi_{R'\Lambda'}(\vec{r}) \Phi_{R\Lambda}^\dagger(\vec{r}) \vec{\alpha} \right] \\ &= ec \sum_{R\Lambda, R'\Lambda'} G_{R'\Lambda', R\Lambda}^< \Phi_{R\Lambda}^\dagger(\vec{r}) \vec{\alpha} \Phi_{R'\Lambda'}(\vec{r}), \end{aligned} \quad (27)$$

for which the computation with the FR-EMTO method is straightforward (for the current density of system with atomic disorders, it is similar to the derivation of disorder-averaged spin current in the next subsection). Then the total current can be given by the integration

$$I = \int dE \int_S \vec{J}(E, \vec{r}) \cdot d\vec{s}. \quad (28)$$

Alternatively, as shown in Appendix B, with the charge conservation law, the total electron-charge current flowing through the central device region can be calculated as the flowing-out current from the left electrode given by the relation

$$I_{\text{total},l} = \frac{e}{\hbar} \int T(E) (f_r - f_l), \quad (29)$$

where  $T(E) = \text{Tr}[G_{CC}^R \Gamma_r G_{CC}^A \Gamma_l]$  is called the transmission coefficient, the linewidth function  $\Gamma_{l/r}^a = i(\Sigma_{l/r}^{a,A} - \Sigma_{l/r}^{a,R})$  characterizing the couplings between electrodes and the central device [50]. The above equation, for fully relativistic quantum transport with the same form as the scalar-relativistic case [26], is known as the Landauer-Buttiker current formula [50]. For the disordered electronic device, we compute the disorder average of the transmission coefficient, namely  $\langle T(E) \rangle = \text{Tr}[\overline{G_{CC}^R \Gamma_r G_{CC}^A \Gamma_l}]$ , which involves the disorder average of two-GF correlators. Here we apply the technique of nonequilibrium vertex correction (NVC) in CPA with SSA, by writing

$$\overline{T}(E) = \mathcal{G}_{CC}^R \Gamma_r \mathcal{G}_{CC}^A \Gamma_l + \mathcal{G}_{CC}^R \Omega_{NVC} \mathcal{G}_{CC}^A \Gamma_l \quad (30)$$

(for more details, please refer to our previous works in Refs. [26,38,51,52]). The first term is usually called coherent part accounting for the contribution of momentum coherent transport through the effective medium. The NVC  $\Omega_{NVC}$  provides an effective way to account for the effects of multiple scattering of disorders, presenting an important way to simulate the realistic device with inevitable random defects/impurities [26,38,51,53]. In our present implementation of the FR-EMTO, in addition to disorder effects, the fully relativistic effects are included for quantum transport simulation of disordered nanoelectronics, significantly extending the capability of first-principles device-material simulation.

### B. Electronic spin transport: Pauli spin current

The spin current is one of main concerns in the field of the spintronics. To study the spintronic phenomena, the central task is to calculate the time evolution of the spin polarization density defined as  $\vec{S} = \frac{1}{2} \Psi^\dagger \vec{\Sigma} \Psi$ , namely to calculate  $\frac{d}{dt} \vec{S}$ . (Note that in relativistic quantum mechanics, the general definition of the spin polarization operator is still an important issue [54,55]. Here we use the Pauli spin operator for low-energy physics of condensed-matter materials.) As we shown in Appendix C, we can obtain the continuity relation

$$\frac{d}{dt} \vec{S} = -\nabla \cdot \vec{J}^s + \frac{i}{\hbar} \Psi^\dagger [\hat{H}, \vec{\Sigma}] \Psi, \quad (31)$$

where  $\vec{J}^s$  is the spin current density tensor and  $\frac{i}{\hbar} \Psi^\dagger [\hat{H}, \vec{\Sigma}] \Psi$  is the torque term. Here, the spin current tensor element  $J_j^s$ , for the spin's  $i$ th component transporting in the  $j$ th direction, is given as

$$J_j^s(\vec{r}) = \frac{1}{2} [c \Psi^\dagger(\vec{r}) \alpha_j \Sigma_i \Psi(\vec{r}')]_{\vec{r}=\vec{r}'}, \quad (i, j = x, y, z). \quad (32)$$

We also find that the definition of spin current in Eq. (32) can be derived from quantum electrodynamics with the Noether theorem [56]. As demonstrated in Ref. [56], in the non-relativistic limit up to the order of  $\frac{1}{c}$ , the spin current in Eq. (32) not only contains the conventional spin current,

namely  $\frac{1}{2}(\hat{v}\sigma + \sigma\hat{v})$ , but also contains an important contribution  $\frac{i}{2}[(\sigma \times \hat{v})\sigma + \sigma(\hat{v} \times \sigma)]$  (due to the SOI) which is responsible for the spin Hall effect.

We note that the overlapping FR-EMTO presents an important difficulty for implementing the local current formalism for calculating the spin current [57–59]. In this work, based on the NEGF and FR-EMTO method, we present the real-space technique for first-principles calculation of the Pauli spin current density as

$$\begin{aligned} J_j^{s_i}(E, \mathbf{r}) &= \frac{c}{2} \text{Tr}[\Psi(\vec{r})\Psi^\dagger(\vec{r}')\alpha_j \Sigma_i]_{\vec{r}=\vec{r}'} \\ &= -\frac{ic}{4\pi} \text{Tr}[G^<(\vec{r}, \vec{r}')\alpha_j \Sigma_i]_{\vec{r}=\vec{r}'} \\ &= -\frac{ic}{4\pi} \text{Tr} \left[ \sum_{R\Lambda, R'\Lambda'} G_{R'\Lambda', R\Lambda}^< \Phi_{R'\Lambda'}(\vec{r})\Phi_{R\Lambda}^\dagger(\vec{r}')\alpha_j \Sigma_i \right] \\ &= -\frac{ic}{4\pi} \sum_{R\Lambda, R'\Lambda'} G_{R'\Lambda', R\Lambda}^< \Phi_{R\Lambda}^\dagger(\vec{r}')\alpha_j \Sigma_i \Phi_{R'\Lambda'}(\vec{r}). \end{aligned} \quad (33)$$

For a disordered system, the disorder-averaged spin current density can be calculated with the conditionally averaged NEGF as follows (for more details, see Appendix C):

$$\begin{aligned} \bar{J}_j^{s_i} &= -\frac{ic}{4\pi} \left[ \sum_{R\Lambda R'\Lambda'} \sum_Q C_R^Q \mathcal{G}_{R'\Lambda', R\Lambda}^{<, Q} \Phi_{R\Lambda}^{Q, \dagger} \alpha_j \Sigma_i \Phi_{R'\Lambda'}^Q \right. \\ &\quad \left. + \sum_{R\Lambda R'\Lambda'} \sum_{Q'Q} C_R^{Q'} C_{R'}^{Q'} \mathcal{G}_{R'\Lambda', R\Lambda}^{<, Q'Q} \Phi_{R\Lambda}^{Q, \dagger} \alpha_j \Sigma_i \Phi_{R'\Lambda'}^{Q'} \right], \end{aligned} \quad (34)$$

where  $\mathcal{G}^{<, Q'Q}$  is defined in Eq. (26) with the CPA. Then with the spin current density, the total Pauli spin current through a surface area can be directly obtained by the integration  $I^{s_i} = \int dE \int_S \bar{J}^{s_i}(E, \vec{r}) \cdot d\vec{s}$ . For a closed surface, the total spin current provides the spin-torque contribution, due to spin current flow, to the enclosed region. The use of the compact basis set, FR-EMTO, can greatly reduce the computational cost for spin current density. By calculating the spin current from first principles, the various spin-transport phenomena can be analyzed for spintronic device materials. Importantly, with the FR-EMTO method, the effects of random impurities and defects on spin transport can be effectively calculated. Moreover, it should be mentioned that with the real-space technique, the computation of the torque term in Eq. (31) is also straightforward in the FR-EMTO method for both ordered and disordered devices with the NEGF technique, which are going to be reported in our next work. Here, it is worth mentioning that according to the Helmholtz theorem, a unique definition of spin current in a device system, as shown in Fig. 1, depends on the boundary conditions, divergence and circulation of the current. As shown in Appendix C, not like the divergence, the circulation is not definitely defined for spin current. However, the present definition of spin current in Eq. (32) is physically transparent, and possesses the correct divergence of current needed for calculating  $\frac{d\vec{S}}{dt}$  which is physically important. For the boundary condition in our

present calculation, we use the nearly spin-current-conserved electrodes in which the SOI is negligible.

## VI. IMPLEMENTATION AND RESULTS

We have implemented the FR-EMTO-based KSDFT in a first-principles nanoelectronic device simulation package including both the bulk- and device-materials solvers. For the electronic structure self-consistent calculation, please refer to Ref. [18] for the quantities including electron charge density and spin density inside each atomic sphere. For the intercell electrostatic potential in the effective muffin-tin potential, we use the spherical cell approximation proposed by Vitos [23,25], and the detailed treatment of the Madelung potential for device structures can be found in Ref. [26]. In our present implementation for device structures, the renormalization of spherical cell approximation (SCA) charge to neutrality for the central device region is realized by introducing the site-dependent shift  $\delta Q_R$  which is determined by the on-site elements of the normalized Green's function (namely  $G \cdot O$ ). The Anderson mixing algorithm is applied for the self-consistency in the present implementation. In the calculations of charge density and charge- and spin-current density, we use  $l_{\max} = 8$  in the expansion of SSW in Eq. (8). In this section, we demonstrate the correctness of our numerical implementation of FR-EMTO by investigating both the electronic structure and transport properties of device and bulk materials. To test the bulk material solver, we calculate the spectra function of FCC Co, Pt, and HgTe and compare with the band structure of PAW calculations with VASP [12]. Moreover, as a test of the electronic structure calculation with the device-material solver, we calculate the Rashba-type surface states of the FCC Au(111) surface and FCC Ag(111)/Ag<sub>2</sub>Bi<sub>1</sub> alloy surface, and the FR-EMTO results are compared with the experimental measurements and the PAW slab calculations [12]. For an ordered system, to get the spectral function, we calculate the normalized GF for each  $\vec{k}$  at the energy  $E$ ,

$$A_B(z, \vec{k}) = -\frac{1}{\pi} \text{Im}[G^{\mathcal{R}}(z, \vec{k})O(z, \vec{k})]_{BB}, \quad (35)$$

where  $B$  is the basis site in a primitive/unit cell. (Please refer to Appendix D for the spectra function of disordered systems.) For the quantum transport properties, we mainly investigate the charge and the spin transport in the perfect and disordered Cu/Co/Pt/Cu junctions, and the effects of disorders and interfaces on the transport are calculated from first principles. In the bulk and two-probe electronic structure calculations, to ensure the convergence, we use 30 energy points for the complex energy contour with the Gaussian quadrature method, and  $60 \times 60 \times 60$  and  $60 \times 60$  uniform  $k$  meshes for the bulk 3D and device 2D whole first Brillouin zones (BZs), respectively. The local spin density approximation (LSDA) exchange-correlation functional [60] is employed in our calculations of both spin-polarized and nonpolarized material systems. In the calculation of the transmission coefficient, a  $200 \times 200$   $k$  mesh is used for the plot in the whole 2D BZ. For the real-space charge current density and spin-current density, a  $100 \times 100$   $r$  mesh is used for the integration and plot. For more details, please refer to the Supplemental Material [61].

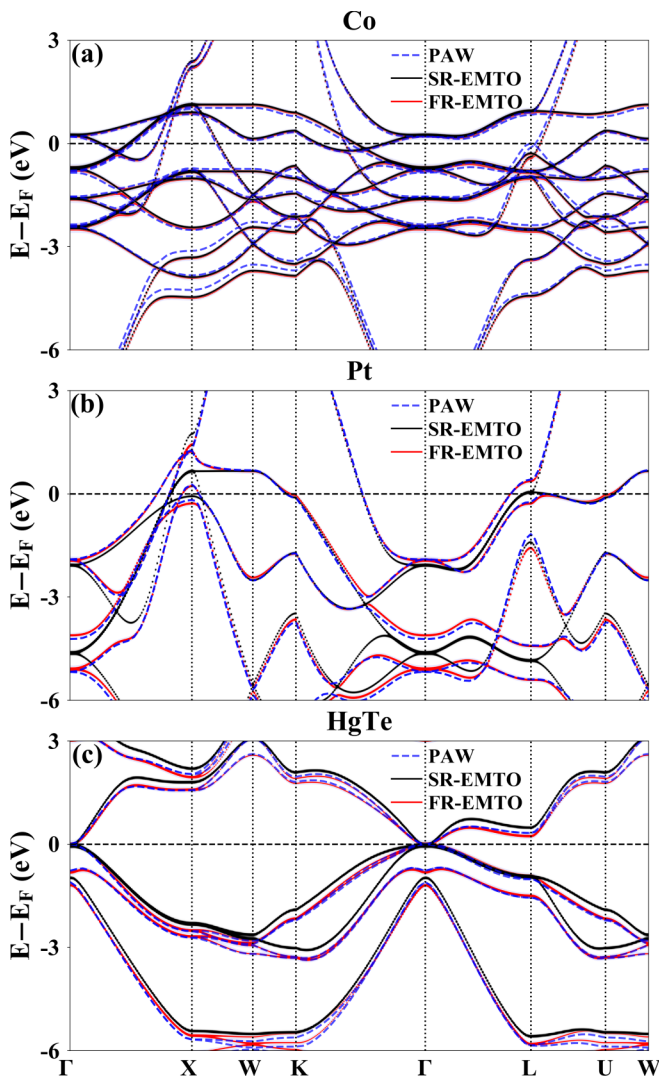


FIG. 2. Electron dispersion of bulk Co (a), Pt (b), and HgTe (c). Yellow dashed line: Result of PAW with SOI. Black solid line: Result of SR-EMTO. Red solid line: Result of FR-EMTO.

### A. Fully relativistic electron dispersion of bulk Co, Pt, and HgTe

First of all, we demonstrate the implementation of the FR-EMTO-based bulk solver for the electronic structures of bulk materials. We calculate the spectral function for the bulk FCC structures of Co, Pt, and HgTe (see the Supplemental Material for the computation details [61]). Figure 2 presents the FR-EMTO electron dispersion results together with the calculations of SR-EMTO and PAW for comparison. As shown in Fig. 2, despite the very different ways for including the relativistic effects, the implemented FR-EMTO (in red) presents very good agreement with the calculations of PAW (in dashed blue) for all the calculated bulks (especially in the range  $\pm 3$  eV around the Fermi energy  $E_F = 0.0$  eV), demonstrating the important accuracy of the FR-EMTO method. As known, the relativistic effect generally becomes more and more important when the atomic number and electron angular momentum increases. As seen in Fig. 2(b) for Pt and Fig. 2(c) for HgTe, the FR-EMTO and PAW results present important band splitting compared to the results of SR-EMTO (in black)

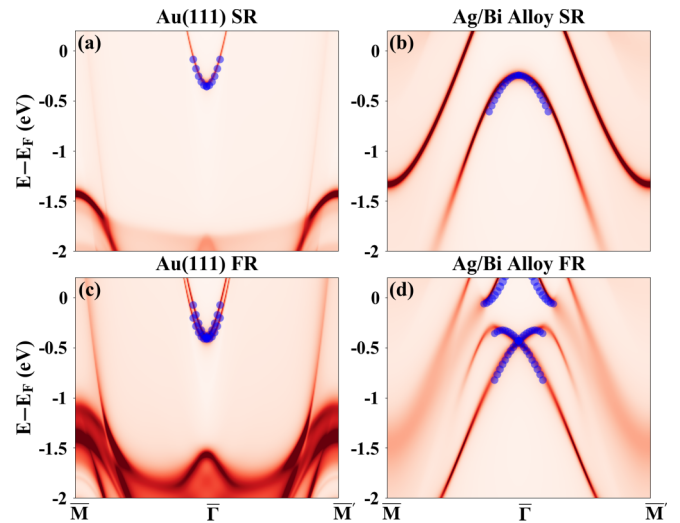


FIG. 3. The electron dispersion of the Rashba-type surface states for Au(111) and Ag(111)/(1ML)Ag<sub>2</sub>Bi<sub>1</sub> alloy surfaces. Blue circles: PAW slab calculations with VASP code.

where the SOI is neglected. In particular, for Pt at the  $\Gamma$  point, the single band at  $E = -4.70$  eV in SR-EMTO is split into two bands with an interval  $\Delta E = 0.96$  eV with FR-EMTO, reproducing very well the results of PAW. In comparison with Pt, the effect of SOI in HgTe is relatively smaller, but not negligible, because of the smaller atomic number of Te compared to Pt, and the fact that states in Hg feature low angular momentum around the Fermi energy. In Co, it is clear that both spin-polarized FR-EMTO and PAW calculations present almost the same results as the SR-EMTO calculation, presenting the fact that the SOI is very weak in bulk Co. Here, it should be mentioned that in the present implementation of FR-EMTO, the major error source is the spherical cell approximation used to simplify the calculation of the intercell electrostatic interaction. However, the present EMTO method features the important advantages of the overlapping potential sphere and equal-footing treatments of atomic and interstitial regions, and thus is expected to provide high accuracy for simulating electronic device materials with surfaces/interfaces, beyond the second-generation TB-LMTO method.

### B. Rashba-type states of Au and Ag/Ag<sub>2</sub>Bi<sub>1</sub> alloy (111) surfaces

To validate our implementation of the FR-EMTO for device materials, we study the electronic structures of the Au(111) surface and Ag(111)/(1ML)Ag<sub>2</sub>Bi<sub>1</sub> alloy surface, in which Rashba-type spin splitting has been experimentally measured due to the strong SOI on both surfaces [62–66]. In the EMTO calculation, the electronic structure is self-consistently obtained with the two-probe device structure, namely Au/(12ML)vacuum/Au, and Ag/(1ML)Ag<sub>2</sub>Bi<sub>1</sub>/(12ML)vacuum/Ag with transport direction of FCC(111). As a comparison, we also conduct band structure calculations for Au(111) and Ag/(1ML)Ag<sub>2</sub>Bi<sub>1</sub> surfaces by using VASP based on slab structures (for more details, see the Supplemental Material) [12]. In our calculation, the surface atomic layer is fully relaxed with VASP. Figure 3 presents electron dispersion of the surface layer calculated by

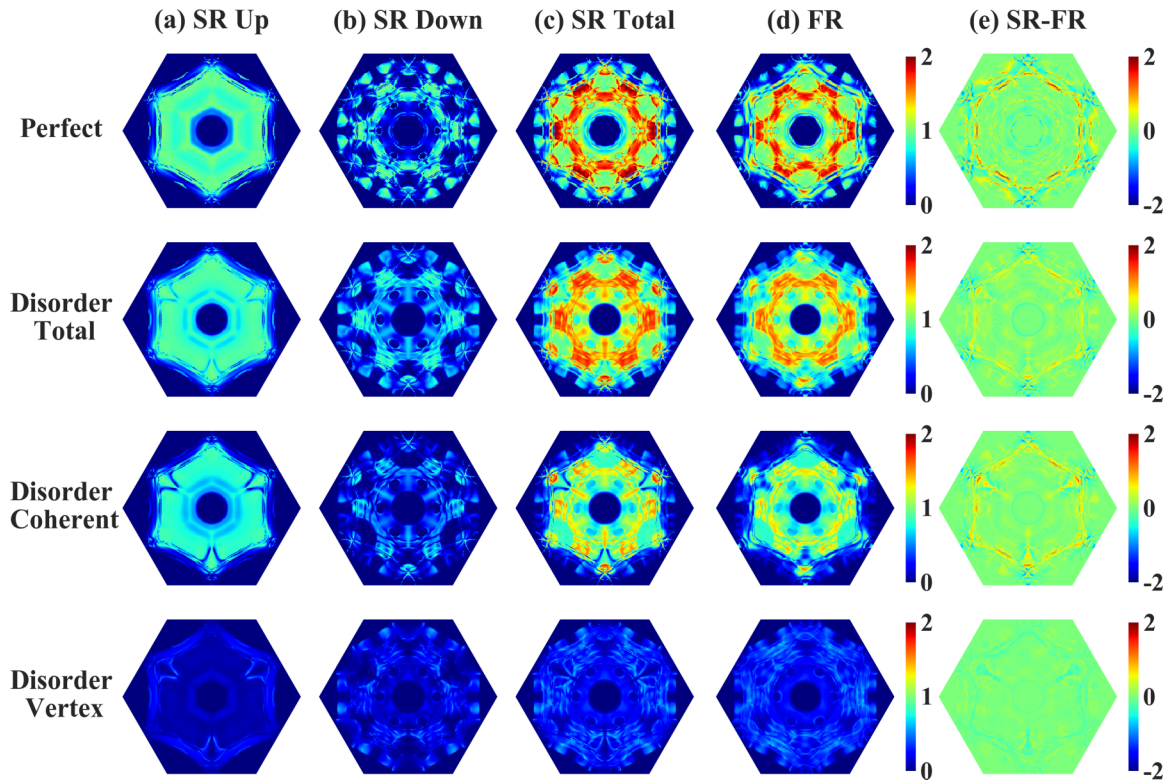


FIG. 4.  $k_{\parallel}$ -resolved transmission coefficient  $\mathcal{T}(k_{\parallel})$  in two-dimensional BZ for the perfect Cu/(8ML)Co/(5ML)Pt/Cu junction, and Cu/(7ML)Co(1ML)Co<sub>0.5</sub>Pt<sub>0.5</sub>/(5ML)Pt/Cu junction with interfacial disorder: (a) SR spin-up channel, (b) SR spin-down channel, (c) SR total, (d) FR total, and (e) difference between SR and FR calculations.

both SR- and FR-EMTO methods in comparison with PAW slab calculations with and without SOI (blue circles). It is clear that surface states calculated by EMTO methods agree well with those calculated by VASP, presenting an important test for our first-principles implementation of EMTO. For both Au(111) and Ag/(1ML)Ag<sub>2</sub>Bi<sub>1</sub> surfaces, as shown in Figs. 3(c) and 3(d), the results of FR-EMTO and VASP with SOI present apparent spin splitting in the parabolic surface bands around the  $\Gamma$  point, which is absent in the calculations without SOI [see Figs. 3(a) and 3(b)]. Such band splittings, known as the “Rashba effect,” are caused by inversion symmetry breaking in surface structures and the strong SOI.

It should be mentioned that the SOI is very weak in the bulk Au around the  $E_F$  due to the dominant  $s$  orbital ( $l = 0$ ). However, as shown in the SR-EMTO result of Fig. 3(a), the Au(111) surface presents an interesting parabolic band (close to the  $E_F$ ) with the dominant component of the  $p$  orbital ( $l = 1$ ). For such surface state, the inclusion of SOI can give rise to appreciable Rashba-type spin splitting as shown in FR-EMTO calculation. It can be measured that the Rashba constant for the parabolic state is  $\alpha_R = 0.35$  eV/Å with FR-EMTO, agreeing well with previous experimental measurement [62–64] and VASP calculation (0.38 eV/Å). For the Ag/Ag<sub>2</sub>Bi<sub>1</sub> alloy surface, we calculate the long-range ordered ( $\sqrt{3} \times \sqrt{3}$ )R30° structure with 2 Ag and 1 Bi atoms, and the surface Bi atoms located 0.60 Å above the surface Ag atoms, consistently with previous experimental and theoretical studies [65,66]. As shown in Figs. 3(c) and 3(d), the Ag/Ag<sub>2</sub>Bi<sub>1</sub> surface with FR-EMTO presents a giant Rashba-type spin splitting

for the parabolic surface state around the  $\Gamma$  point, much larger than that of the Au(111) surface. It is calculated that, for the spin splitting, the giant Rashba constant is  $\alpha_R = 2.7$  eV/Å, agreeing well with experimentally measured value of 3.0 eV/Å [65]. The successful reproduction of the Rashba-type surface states on Au(111) and Ag/(1ML)Ag<sub>2</sub>Bi<sub>1</sub> surfaces presents an important test for FR-EMTO electronic structure calculation of the device materials, providing an important basis for the fully relativistic quantum transport simulation from first principles. In the following, we investigate the electronic charge and spin transport through different interfaces to demonstrate the FR-EMTO-based first-principles quantum transport method.

### C. Electronic charge transport

For the transport, we calculate the electron transmission coefficients with FR-EMTO and compare with the results of SR-EMTO calculations [26]. Figure 4 presents the  $k_{\parallel}$ -resolved transmission for the perfect and disordered junctions of Cu/Co/Pt/Cu with transport in the FCC(111) direction (see the Supplemental Material for the transport results of the Pt(111)/Al(111) and Co(111)/Co(111) systems [61]). As shown in the first row of Fig. 4 for the perfect junction, it can be found that the result of FR-EMTO possesses a 3-fold symmetry, while the SR-EMTO results possess a 6-fold symmetry for both spin-up and spin-down channels. However, as shown in the Supplemental Material, the perfect Pt/Al asymmetric heterostructure presents a 6-fold symmetry for both the

FR- and SR-EMTO calculations. It has been known that the 6-fold symmetry in the FR-EMTO calculation of perfect Pt/Al and all the SR-EMTO calculations is given by the 3-fold geometry symmetry in FCC(111) plus the time-reversal symmetry [namely the relation  $T(k_{\parallel}) = T(-k_{\parallel})$ ] for the ordered devices in the absence of both SOI and spin polarization [67]. However, for the perfect Co/Pt, spin-polarization in Co and strong SOI in Pt break the time-reversal symmetry in the FR-EMTO calculation, resulting in the different symmetry compared to SR-EMTO results. Moreover, in contrast to the FR-EMTO calculation of magnetically perfect Cu/Co/Pt/Cu, we find that the Sharvin transmission of Co/Co presents a 6-fold symmetry in FR-EMTO calculations as shown in the Supplemental Material [61]. Here, the 6-fold symmetry in FR results of Co/Co is attributed to the translational symmetry of FCC(111) in pure Co/Co; namely, the translation along FCC(111) for one layer is equivalent to a 6-fold rotation.

Figure 4(e) shows the difference between FR- and SR-EMTO total transmission, namely  $T^{SR}(k_{\parallel}) - T^{FR}(k_{\parallel})$ . It is clear that the inclusion of SOI (as the major difference in SR and FR calculations) presents the important difference in transmission distribution in the BZ. For example, the transmission difference between FR and SR calculations can be as large as 2.0 in the red circle in Fig. 4(e) for perfect Cu/Co/Pt/Cu. However, we note that the total transmissions of FR and SR are close for all the systems calculated in this work (see the Supplemental Material for Pt/Al and Co/Co results [61]), for example  $T^{FR} = 0.70$  compared to  $T^{SR} = 0.74$ , due to the relatively weak SOI in these systems. The presence of correct symmetry in the FR results and the close total transmission to SR results in various perfect systems presents important tests on the fully relativistic quantum transport method.

As an important capability of the EMTO-based first-principles quantum transport method, the diffusive electron transport through disordered impurities/alloys can be calculated with CPA combining with vertex correction [see Eq. (30)] [38]. The second row of Fig. 4 presents the total transmission results for disordered Cu/(7ML)Co/(1ML)Co<sub>0.5</sub>Pt<sub>0.5</sub>/(5ML)Pt/Cu containing 1 atomic monolayer disordered intermixed interface. It is clearly seen that the results of both SR- and FR-EMTO (including the total, coherent, and vertex correction parts) feature the 3-fold symmetry, contrasting to 6-fold symmetry in SR calculation of the perfect systems. The loss of 6-fold symmetry in the SR coherent part is due to the fact that the effective Hamiltonian with CPA is non-Hermitian, namely the coherent  $\mathcal{D}$  function, and diffusive scattering in disordered devices breaks the symmetry  $T_{R \rightarrow L}^{SR}(\vec{k}_{\parallel}) = T_{L \rightarrow R}^{SR}(\vec{k}_{\parallel})$ , breaking the symmetry  $T(k_{\parallel}) = T(-k_{\parallel})$  [67]. As we find, the presence of 1ML Pt<sub>0.5</sub>Co<sub>0.5</sub> on the interface slightly increases the total transmission in both the SR and FR calculations compared to the results of perfect structure, for example,  $T_{\text{disorder}}^{FR} = 0.71$  and  $T_{\text{disorder}}^{SR} = 0.75$ . Compared to the concentrated pattern in the results of a perfect system, the transmission of the disordered junction becomes more diffusive due to random disorder scattering. In the simulation of disordered devices, we use the coherent part to include electron coherent transport through effective medium without  $\vec{k}_{\parallel}$  relaxation (the third

row in Fig. 4), and use the vertex part to account for the contribution of interchannel diffusive scattering (the fourth row in Fig. 4). Due to the fact that the interchannel scattering induced by 1ML disorder is limited, the vertex correction part is smaller than the coherent part in all FR and SR calculations in Fig. 4. However, the vertex correction is not negligible and has an important contribution to the total transmission, for example,  $T_{\text{vertex}}^{FR} = 0.22$  compared to  $T_{\text{coherent}}^{FR} = 0.49$ . Therefore, we believe that the implementation of the FR-EMTO-based quantum transport method can significantly expand the capability for simulation of realistic nanoelectronics from first principles.

In addition to the reciprocal-space transmission coefficient calculation, we have also implemented the fully relativistic charge current density in real space, as an important test for the real-space transport formalism [see Eq. (27)]. As shown in Fig. 5, we plot the FR current density  $J_z(E_F, \vec{r})$  through a unit cross section at different  $z$ , for both perfect and disordered (with 1ML interfacial Co<sub>0.5</sub>Pt<sub>0.5</sub>) junctions. It is notable that all the real-space current density for both ordered and disordered systems features the 3-fold symmetry. Compared to results of the perfect junction, the presence of disorder at the Co/Pt interface only significantly influences the current density distribution close to the disordered layer, such as the result at  $z_0$ , while  $J_z$  at other places are only slightly tuned. For both the perfect and disordered systems, it is clear that the current density pattern is quite different in different materials due to the different electronic states for the transport. Although there are notable differences in the distribution of current density around the interface and inside different materials Pt, Co, and Cu, we find the integrated total current, namely  $I^{FR} = \int_S J_z dS$ , is the same at different  $z$ , regardless of the numerical error. Moreover, the integrated value equals the total transmission coefficient. In particular, we obtain, for a perfect junction,  $I_{\text{clean}}^{FR,z} = T_{\text{clean}}^{FR} = 0.70$ , and for a disordered junction,  $I_{\text{disorder}}^{FR,z} = T_{\text{disorder}}^{FR} = 0.71$  ( $z = -14, -8, -4, 0, 3, 5, 11$ ). Correctly reproducing the reciprocal-space transmission results demonstrates the correct implementation of the FR-EMTO based real-space transport formalism and the CPA based Keldysh NEGF formalism for the disordered systems. Moreover, due to the similarity between charge current density in Eq. (27) and Pauli spin current density in Eq. (33), the correct implementation of FR charge current density provides an important basis for calculating the Pauli spin current in device materials.

#### D. Electronic spin transport

On the basis of charge current density calculation, the implementation of Pauli spin current density is straightforward, namely by replacing  $c\vec{\alpha}$  with  $c\vec{\alpha}\vec{\Sigma}$  [see Eqs. (33) and (27)]. Here, as further study, we calculate the spin transport in the perfect and disordered Cu/Co/Pt/Cu junctions to demonstrate the important capability of FR-EMTO for the simulation of spintronic device materials. To evaluate the influence of the interface and disorders on the spin transport, Fig. 6 presents the total spin current  $J_z^{s_z}(E_F)$  through the unit cross sections at different  $z$  (we note the nonzero  $J_z^{s_x}$  and  $J_z^{s_y}$  are too small to present here). Here, we set the electron injection from the left Cu electrode by using the electrodes'  $f_L = 1.0$  and  $f_R = 0.0$  in the Keldysh NEGF calculation. It is

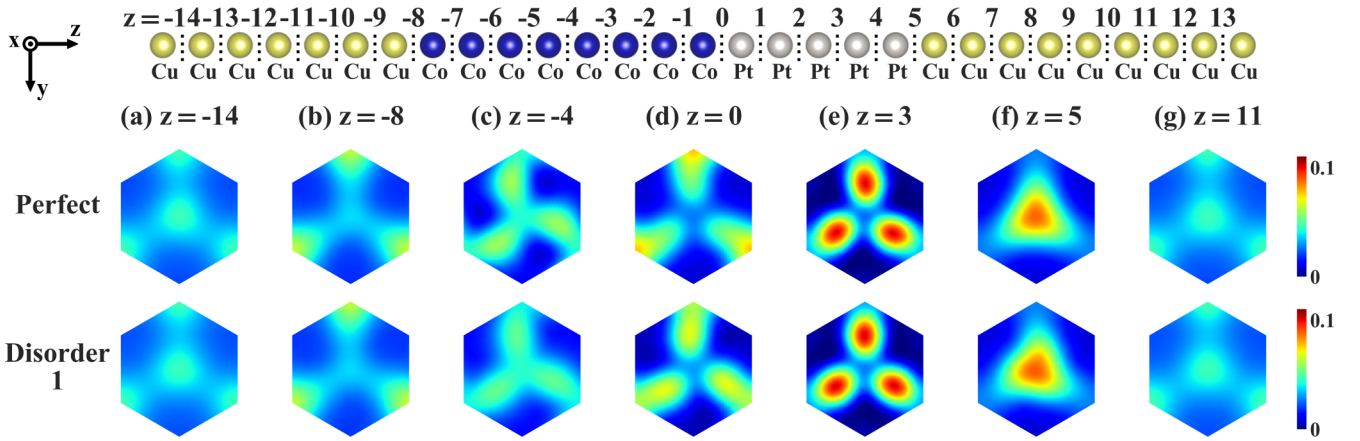


FIG. 5. Current density  $J_z(E_F, \vec{r})$  distribution in the unit cross section perpendicular to transport direction at different  $z$  for the perfect Cu/(8ML)Co/(5ML)Pt/Cu junction in first row, and disordered Cu/(7ML)Co/(1ML)Co<sub>0.5</sub>Pt<sub>0.5</sub>/(5ML)Pt/Cu junction in second row. Each  $z$  is at middle position of two neighboring atomic layers, and  $z = 0$  is set for the Co/Pt interface.

known that the spin current is not conserved in the presence of both the SOI and various scatterings in the FR calculation. In the system Cu/Co/Pt/Cu, the SOI can be negligible inside Cu, but can play an important role for spin transport inside Pt and at the interfaces Co/Pt and Pt/Cu (for the Rashba-type SOI due to the break of inversion symmetry). As a result, for all the three junctions as shown in Fig. 6, the spin current stays almost constant inside the Cu (for  $z \leq -7$  and  $z \geq +6$ ) and presents important variation around the interfaces and inside Pt (for  $-1 \leq z \leq 5$ ). It can be found that as spin current is injected into Pt, the spin current features an appreciable decrease from  $z = -1$  to  $z = 4$  due to the strong SOI at the Co/Pt interface and inside Pt, giving rise to a significant spin memory loss which is consistent with previous studies [68,69]. For the perfect junction (in the red circle), we can find that there exists sharp oscillations inside

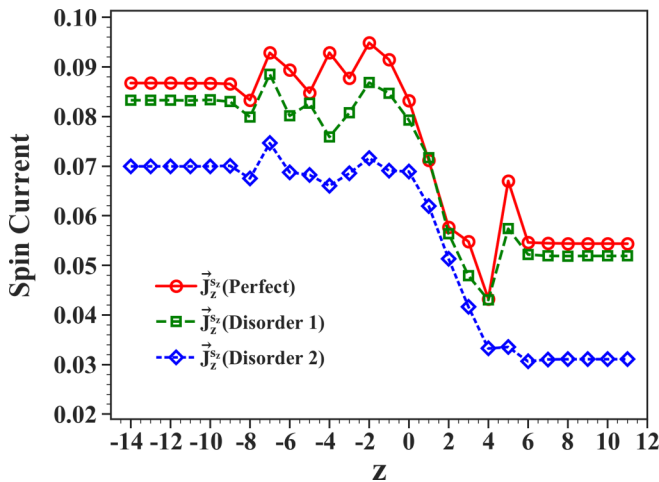


FIG. 6. The total spin current  $J_z^s(E_F)$  through the unit cross section at different  $z$  for energy at  $E_F$ . Red circle: Perfect Cu/(8ML)Co/(5ML)Pt/Co junction. Green square: Disordered Cu/(7ML)Co/(1ML)Co<sub>0.5</sub>Pt<sub>0.5</sub>/(5ML)Pt/Cu junction. Blue diamond: Disordered Cu/(7ML)Co/(1ML)Co<sub>0.5</sub>Pt<sub>0.5</sub>/(5ML)Pt<sub>0.95</sub>Va<sub>0.05</sub>/Cu junction. For structure, see Fig. 5.

Co and at the Pt/Cu interface which can be attributed to the wave-function interference effects in the coherent transport regime. Compared to the results for the perfect junction, the inclusion of 1ML Co<sub>0.5</sub>Pt<sub>0.5</sub> (in the green square) only slightly reduces the inflow and outflow spin current. However, it is apparent that the diffusive scattering induced by the 1ML intermixed layer can significantly modulate the spin current behavior inside the Co and at the sharp Pt/Cu interface. As further introducing 5% disordered vacancies into the 5ML Pt (in the blue diamond), namely Pt<sub>0.95</sub>Va<sub>0.05</sub>, the total spin current at different  $z$  is significantly reduced. In particular, the outflow/inflow spin currents change from the value 0.11/0.17 of the perfect junction to 0.06/0.14 of the disordered junction with Pt<sub>0.95</sub>Va<sub>0.05</sub>. It is clear that more diffusive scattering in Pt<sub>0.95</sub>Va<sub>0.05</sub> greatly smoothens spin current inside Co and at the Pt/Cu interface, and enhances the spin loss (namely reduces the outflow/inflow ratio), presenting the important effects of diffusive disorder scattering on spin transport.

Moreover, Fig. 7 presents the real-space spin current density  $\vec{J}_z^s(\vec{r}, E_F)$  across a 2D unit cell at Fermi level for the different  $z$  (the same as those in charge current density calculations in Fig. 5). For all the cases,  $\vec{J}_z^s(\vec{r}, E_F)$  possesses 3-fold symmetry for both ordered and disordered junctions. It is clear that for each junction, the spin-current distribution is quite different inside different materials and at different interfaces due to the different local states for electron transport. Compared to the results of the perfect junction, the presence of disorders (see the second and third rows in Fig. 7) can greatly modulate the spin current distribution pattern, especially around the Co/Pt interface  $z = -4, 0, 3$ . For example, the sharp peak (the red region) at the corner for the perfect junction is significantly reduced by the presence of the disorders Co<sub>0.5</sub>Pt<sub>0.5</sub> and Pt<sub>0.95</sub>Va<sub>0.05</sub>. In addition, as an important feature of spin transport, the spin current can be negative in some part of the region, presenting the dominant contribution of spin-down electrons. The implementation of the FR-EMTO quantum transport method provides us the important capability to analyze the effects of interface and disorder scatterings on various spin transport phenomena from first principles.

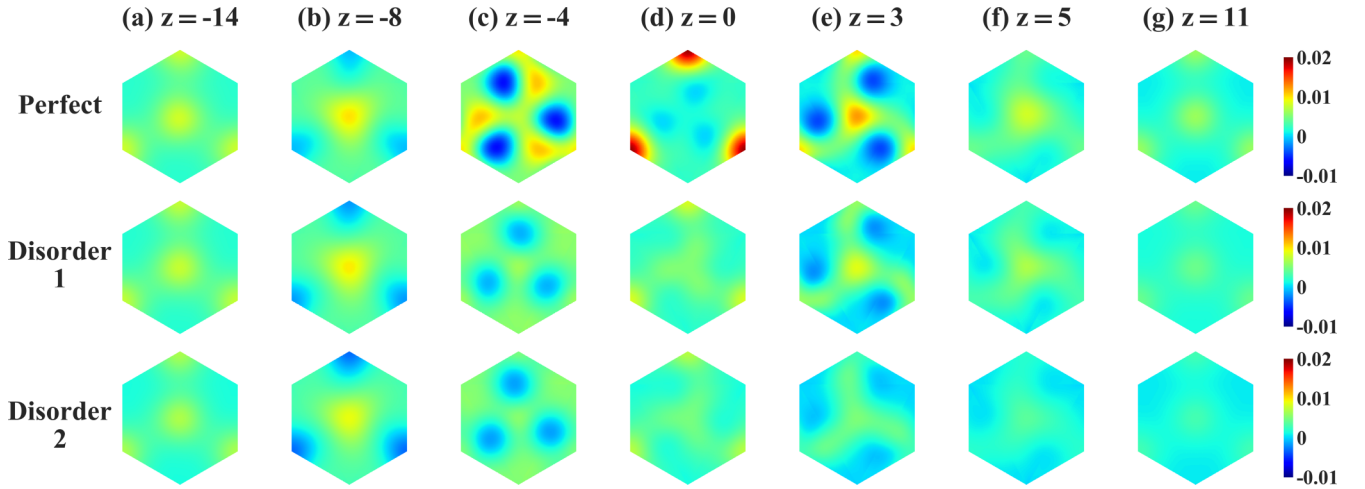


FIG. 7. Real-space spin current density for perfect Cu/(8ML)Co/(5ML)Pt/Cu junction in first row, disordered Cu/(7ML)Co/(1ML)Co<sub>0.5</sub>Pt<sub>0.5</sub>/(5ML)Pt/Cu junction in second row, and disordered Cu/(7ML)Co/(1ML)Co<sub>0.5</sub>Pt<sub>0.5</sub>/(5ML)Pt<sub>0.95</sub>Va<sub>0.05</sub>/Cu junction in third row. For atomic structure, see Fig. 5.

## VII. CONCLUSIONS

In summary, we have implemented the FR-EMTO-based first-principles quantum transport method for simulating the electronic charge and spin transport through device materials. For the device structure, both the spin-polarized and nonpolarized Kohn-Sham Dirac equations are self-consistently solved with the Green's function method. Based on the NEGF technique, we formulate the fully relativistic charge-current/transmission coefficient and Pauli spin current for transport calculation. To treat the disordered defects/impurities inevitable in realistic materials, we combine the NEGF in the Keldysh space with CPA to calculate the disorder-averaged various Green's functions. We account for the effects of the multiple disorder scattering on the transport by vertex corrections to the two-Green's-function correlator. To test our implementation, we investigate the spectra of bulk Co, Pt, and HgTe and Rashba-type spin splitting on the surfaces of FCC Au(111) and Ag(111)/Ag<sub>2</sub>Bi<sub>1</sub>. The results of the first-principles FR-EMTO method agree well with the calculations of projector-augmented wave method in VASP and experimental measurements. For the quantum transport, we calculate the electronic charge and spin transport through perfect and disordered Cu/Co/Pt/Cu junctions, and the important effects of disorder and interface scattering for the spin transport is demonstrated from first principles. The present FR-EMTO-based first-principles quantum transport method provides an important tool for simulating the electron and spin transport properties of realistic device materials, extending the capability of first-principles methods for material simulations.

## ACKNOWLEDGMENTS

Y.K. acknowledges financial support from the ShanghaiTech startup, the NSFC (Grant No. 11874265), and the Innovation Program of the Shanghai Municipal Education Commission (Grant No. 15ZZ114). L.W. acknowledges support from the NSFC (Grant No. 11804266). The authors thank

the HPC platform of ShanghaiTech University for providing the computational facility.

## APPENDIX A: CONDITIONALLY AVERAGED NEGF IN KELDYSH SPACE

For completeness, we here provide some details for deriving the conditionally averaged Keldysh GFs as defined in Eq. (24). We use the occupation operator technique (for more details, please see Ref. [70]).

According to the definition of occupation operator  $\eta_i^Q$ , we can define the random Keldysh quantity for a site  $i$ ,

$$\mathbf{D}_i = \sum_Q \eta_i^Q \mathbf{D}_i^Q, \quad (\text{A1})$$

with the relation

$$\sum_Q \eta_i^Q = 1. \quad (\text{A2})$$

Then, we can solve for  $\eta_i^Q$  ( $Q = A, B$ ),

$$\begin{aligned} \eta_i^A &= -(\Delta \mathbf{D}_i)^{-1} (\mathbf{D}_i^B - \mathbf{D}_i) = -(\mathbf{D}_i^B - \mathbf{D}_i) (\Delta \mathbf{D}_i)^{-1}, \\ \eta_i^B &= (\Delta \mathbf{D}_i)^{-1} (\mathbf{D}_i^A - \mathbf{D}_i) = (\mathbf{D}_i^A - \mathbf{D}_i) (\Delta \mathbf{D}_i)^{-1}, \end{aligned} \quad (\text{A3})$$

where  $\Delta \mathbf{D}_i = \mathbf{D}_i^A - \mathbf{D}_i^B$ . To eliminate the random quantity  $\mathbf{D}_i$ , we use the definitions  $\mathbf{G} = (\mathbf{S} - \mathbf{D})^{-1}$ ,  $\mathcal{G} = (\mathbf{S} - \mathcal{D})^{-1}$  and obtain

$$\mathbf{D} = \mathcal{D} - \mathbf{G}^{-1} + \mathcal{G}^{-1}, \quad (\text{A4})$$

which directly give three identities:

$$\begin{aligned} \langle \mathbf{D} \mathbf{G} \rangle &= \mathcal{D} \mathcal{G}, \quad \langle \mathbf{G} \mathbf{D} \rangle = \mathcal{G} \mathcal{D}, \\ \langle \mathbf{D} \mathbf{G} \mathbf{D} \rangle &= \mathcal{D} \mathcal{G} \mathcal{D} - \langle \mathbf{D} \rangle + \mathcal{D}. \end{aligned} \quad (\text{A5})$$

By substituting Eqs. (A3) and (A4) into the definition of conditionally averaged GFs, namely Eq. (24), and employing the above three identities, we can obtain

$$\bar{\mathbf{G}}_{ii}^Q = (\mathbf{f}_i^Q \mathcal{G})_{ii}, \quad \bar{\mathbf{G}}_{ij}^{QQ'} = (\mathbf{f}_i^Q \mathcal{G} \mathbf{h}_j^{Q'})_{ij}, \quad (i \neq j), \quad (\text{A6})$$

where

$$\begin{aligned} f_i^A &= -\frac{(\Delta \mathcal{D}_i)^{-1}}{c_i^A} (\mathcal{D}_i^B - \mathcal{D}_i), & h_i^A &= -(\mathcal{D}_i^B - \mathcal{D}_i) \frac{(\Delta \mathcal{D}_i)^{-1}}{c_i^A}, \\ f_i^B &= \frac{(\Delta \mathcal{D}_i)^{-1}}{c_i^B} (\mathcal{D}_i^A - \mathcal{D}_i), & h_i^B &= (\mathcal{D}_i^A - \mathcal{D}_i) \frac{(\Delta \mathcal{D}_i)^{-1}}{c_i^B}. \end{aligned} \quad (\text{A7})$$

With the CPA condition  $\langle t_i \rangle = 0$ ,  $f_i^Q$  and  $h_i^Q$  can be rewritten in a more compact form as follows:

$$f_i^Q = 1 + \mathcal{G}_{ii} t_i^Q, \quad h_i^Q = 1 + t_i^Q \mathcal{G}_{ii}. \quad (\text{A8})$$

Then, we obtain the conditionally averaged Keldysh GFs,

$$\bar{\mathcal{G}}_{ii}^Q = (\mathcal{G} + \mathcal{G} t_i^Q \mathcal{G})_{ii}, \quad \bar{\mathcal{G}}_{ij}^{QQ'} = [(1 + \mathcal{G} t_i^Q) \mathcal{G} (1 + t_j^{Q'} \mathcal{G})]_{ij}. \quad (\text{A9})$$

By rewriting the quantities in Eqs. (A9) with the Keldysh representation, namely  $\mathcal{G} = \begin{pmatrix} \mathcal{G}^A & 0 \\ \mathcal{G}^{\mathcal{K}} & \mathcal{G}^{\mathcal{R}} \end{pmatrix}$  and  $t^Q = \begin{pmatrix} t^{\mathcal{K},Q} & 0 \\ 0 & t^{\mathcal{R},Q} \end{pmatrix}$ , we can find

$$\begin{aligned} \bar{g}_{ii}^{A,Q} &= [\mathcal{G}^A + \mathcal{G}^A t_i^{A,Q} \mathcal{G}^A]_{ii}, & \bar{g}_{ii}^{\mathcal{R},Q} &= [\mathcal{G}^{\mathcal{R}} + \mathcal{G}^{\mathcal{R}} t_i^{\mathcal{R},Q} \mathcal{G}^{\mathcal{R}}]_{ii}, \\ \bar{g}_{ii}^{\mathcal{K},Q} &= [\mathcal{G}^{\mathcal{K}} + \mathcal{G}^{\mathcal{R}} t_i^{\mathcal{K},Q} \mathcal{G}^A + \mathcal{G}^{\mathcal{K}} t_i^{A,Q} \mathcal{G}^A + \mathcal{G}^{\mathcal{R}} t_i^{\mathcal{R},Q} \mathcal{G}^{\mathcal{K}}]_{ii}, \end{aligned} \quad (\text{A10})$$

and

$$\begin{aligned} \bar{g}_{ij}^{A,QQ'} &= [(1 + \mathcal{G}^A t_i^{A,Q}) \mathcal{G}^A (1 + t_j^{A,Q'} \mathcal{G}^A)]_{ij}, \\ \bar{g}_{ij}^{\mathcal{R},QQ'} &= [(1 + \mathcal{G}^{\mathcal{R}} t_i^{\mathcal{R},Q}) \mathcal{G}^{\mathcal{R}} (1 + t_j^{\mathcal{R},Q'} \mathcal{G}^{\mathcal{R}})]_{ij}, \\ \bar{g}_{ij}^{\mathcal{K},QQ'} &= [(1 + \mathcal{G}^{\mathcal{R}} t_i^{\mathcal{R},Q}) \mathcal{G}^{\mathcal{K}} (1 + t_j^{A,Q'} \mathcal{G}^A) \\ &\quad + [(\mathcal{G}^{\mathcal{K}} t_i^{A,Q} + \mathcal{G}^{\mathcal{R}} t_i^{\mathcal{K},Q}) \mathcal{G}^A (1 + t_j^{A,Q'} \mathcal{G}^A)]_{ij} \\ &\quad + [(1 + \mathcal{G}^{\mathcal{R}} t_i^{\mathcal{R},Q}) \mathcal{G}^{\mathcal{R}} (t_j^{\mathcal{K},Q'} \mathcal{G}^A + t_j^{\mathcal{R},Q'} \mathcal{G}^{\mathcal{K}})]_{ij}]. \end{aligned} \quad (\text{A11})$$

Then with the above results, all the conditionally averaged GFs can be found with CPA, including  $\mathcal{G}^{<,Q/Q'}$ , to calculate the physical properties of a disordered system.

## APPENDIX B: FULLY RELATIVISTIC ELECTRONIC CHARGE CURRENT FORMULA

To derive the current formula, we can use the time-dependent Dirac equation

$$i\hbar \frac{d}{dt} \Psi = \hat{H} \Psi, \quad (\text{B1})$$

where  $H$  is given in Eq. (1). Then  $-i\hbar \frac{d}{dt} \Psi^\dagger = \Psi^\dagger \hat{H}^\dagger$ , and  $\hat{H}^\dagger = c\vec{p}^\dagger \cdot \vec{\alpha}^\dagger + (\beta - I_4)mc^2 + V(\vec{r}) + \beta \vec{\Sigma} \cdot \vec{B}(\vec{r})$ . One can straightforwardly check that

$$\begin{aligned} q \frac{d}{dt} (\Psi^\dagger \Psi) &= \frac{d}{dt} (\Psi^\dagger) \Psi + \Psi^\dagger \frac{d}{dt} (\Psi) \\ &= -q c (\nabla \Psi^\dagger) \vec{\alpha} \Psi - \Psi^\dagger (q c \vec{\alpha} \cdot \nabla \Psi) \\ &= -\nabla \cdot (q c \Psi^\dagger \vec{\alpha} \Psi) \\ &= -\nabla \cdot \vec{J}, \end{aligned} \quad (\text{B2})$$

where  $c\vec{\alpha} = \frac{i}{\hbar} [\vec{r}, \hat{H}]$  is the velocity operator in FR quantum mechanics, and the current density is given as

$$\vec{J} = q c \Psi^\dagger \vec{\alpha} \Psi. \quad (\text{B3})$$

For the total current, in an alternative way, we consider  $\Psi = \{\Psi_L, \Psi_C, \Psi_R\}$  with the three parts for the respective left electrode, central device region, and right electrode in a orthonormal basis representation. Then we can rewrite the Dirac equation for a two-probe device system,

$$i\hbar \frac{d}{dt} \begin{pmatrix} \Psi_L \\ \Psi_C \\ \Psi_R \end{pmatrix} = \begin{pmatrix} H_L & \tau_L^\dagger & 0 \\ \tau_L & H_C & \tau_R \\ 0 & \tau_R^\dagger & H_R \end{pmatrix} \begin{pmatrix} \Psi_L \\ \Psi_C \\ \Psi_R \end{pmatrix}. \quad (\text{B4})$$

Then one can find that

$$i\hbar \frac{d}{dt} \Psi_L = H_L \Psi_L + \tau_L^\dagger \Psi_C, \quad (\text{B5})$$

$$i\hbar \frac{d}{dt} \Psi_C = \tau_L \Psi_L(\vec{r}, t) + H_C \Psi_C + \tau_R \Psi_R, \quad (\text{B6})$$

$$i\hbar \frac{d}{dt} \Psi_R = \tau_R^\dagger \Psi_C + H_R \Psi_R. \quad (\text{B7})$$

Therefore, we have the following solutions for the left and right electrodes with coupling to the central device:

$$\Psi_L = \Psi_{L,0} + g_{LL} \tau_L^\dagger \Psi_C, \quad (\text{B8})$$

$$\Psi_R = \Psi_{R,0} + g_{RR} \tau_R^\dagger \Psi_C, \quad (\text{B9})$$

where  $i\hbar \frac{d}{dt} \Psi_{L,0} = H_L \Psi_{L,0}$ ,  $i\hbar \frac{d}{dt} \Psi_{R,0} = H_R \Psi_{R,0}$ ,  $(i\hbar \frac{d}{dt} - H_L)g_{LL} = \delta$ , and  $(i\hbar \frac{d}{dt} - H_R)g_{RR} = \delta$ , describing the electrodes disconnecting to the central device. With the above results, we can obtain, for the central part,

$$i\hbar \frac{d}{dt} \Psi_C = (H_C + \Sigma) \Psi_C + S, \quad (\text{B10})$$

with the so-called self-energy  $\Sigma = \tau_L g_{LL} \tau_L^\dagger + \tau_R g_{RR} \tau_R^\dagger$  and the source term  $S = \tau_L \Psi_{L,0} + \tau_R \Psi_{R,0}$  [50]. As an result, we obtain

$$\Psi_C = \Psi_{C,0} + G_{CC} S, \quad (\text{B11})$$

where  $\Psi_{C,0}$  describes the device disconnecting to the electrodes,  $(i\hbar\frac{d}{dt} - H_C - \Sigma)G_{cc} = \delta$ . In practical applications we neglect  $\Psi_{C,0}$  assuming that all the states of central device are perturbed by contacting with electrodes, and thus  $\Psi_C = G_{CC}S$ . Then with these important relations, we can derive that the current flowing from left to right is given by

$$\begin{aligned} \frac{d}{dt}(\Psi_L^\dagger\Psi_L) &= \text{Tr}\left[\frac{d}{dt}(\Psi_L\Psi_L^\dagger)\right] = \text{Tr}\left[\frac{d\Psi_L}{dt}\Psi_L^\dagger + \Psi_L\frac{d\Psi_L^\dagger}{dt}\right] = -\frac{i}{\hbar}\text{Tr}[\tau_L^\dagger\Psi_C\Psi_L^\dagger - \Psi_L\Psi_C^\dagger\tau_L] \\ &= -\frac{i}{\hbar}\text{Tr}[G_{CC}\Sigma_L^< + G_{CC}^<\Sigma_L^\dagger - \Sigma_L^<G_{CC}^\dagger - \Sigma_L G_{CC}^<]. \end{aligned} \quad (\text{B12})$$

In the steady state, it is easier to work with energy-dependent quantities. By doing Fourier transformation, we find that the total current flowing out the left electrode can be obtained with energy integration,

$$\begin{aligned} I_L &= \frac{ie}{\hbar} \int dE \text{Tr}\{\Sigma_L^<(E)[G_{CC}^{\mathcal{R}}(E) - G_{CC}^{\mathcal{A}}(E)] + G_{CC}^<(E)[\Sigma_L^{\mathcal{A}}(E) - \Sigma_L^{\mathcal{R}}(E)]\} \\ &= \frac{e}{\hbar} \int dE \text{Tr}\{\Gamma_L[f_L(E)G_{CC}^{\mathcal{R}}(E)i(\Sigma^{\mathcal{R}} - \Sigma^{\mathcal{A}})G_{CC}^{\mathcal{A}}(E)] + G_{CC}^<(E)\} \\ &= \frac{e}{\hbar} \int dE \text{Tr}[(f_L - f_R)\Gamma_L G_{CC}^{\mathcal{R}}(E)\Gamma_R G_{CC}^{\mathcal{A}}(E)], \end{aligned} \quad (\text{B13})$$

where  $\Gamma_{L/R} = i[\Sigma_{L/R}^{\mathcal{A}}(E) - \Sigma_{L/R}^{\mathcal{R}}(E)]$ ,  $\Sigma^< = \Sigma_L^< + \Sigma_R^< = f_L(E)\Gamma_L + f_R(E)\Gamma_R$ . Here, one can define the transmission coefficient as

$$T(E) = \Gamma_L G_{CC}^{\mathcal{R}}(E)\Gamma_R G_{CC}^{\mathcal{A}}(E). \quad (\text{B14})$$

### APPENDIX C: FULLY RELATIVISTIC PAULI SPIN CURRENT FORMULA

We can check the following continuity relation:

$$\begin{aligned} \frac{d}{dt}\left[\Psi^\dagger\frac{1}{2}\Sigma_i\Psi\right] &= \frac{1}{2}\frac{d}{dt}[\Psi^\dagger]\Sigma_i\Psi + \frac{1}{2}\Psi^\dagger\Sigma_i\frac{d}{dt}[\Psi] = \frac{i}{2\hbar}[\Psi^\dagger\hat{H}^\dagger\Sigma_i\Psi - \Psi^\dagger\Sigma_i\hat{H}\Psi] \\ &= \frac{i}{2\hbar}[\Psi^\dagger\hat{H}^\dagger\Sigma_i\Psi - \Psi^\dagger\hat{H}\Sigma_i\Psi] + \frac{i}{2\hbar}\Psi^\dagger[\hat{H}, \Sigma_i]\Psi = \frac{i}{2\hbar}(\vec{p}\Psi)^\dagger c\vec{\alpha}\Sigma_i\Psi - \frac{i}{2\hbar}\Psi^\dagger c\vec{\alpha}\Sigma_i \cdot \vec{p}\Psi + \frac{i}{2\hbar}\Psi^\dagger[\hat{H}, \Sigma_i]\Psi \\ &= -\frac{1}{2}[\nabla\Psi^\dagger]c\vec{\alpha}\Sigma_i\Psi(\mathbf{r}) - \frac{1}{2}\Psi^\dagger c\vec{\alpha}\Sigma_i\nabla[\Psi] + \frac{i}{2\hbar}\Psi^\dagger[\hat{H}, \Sigma_i]\Psi = -\frac{1}{2}\nabla \cdot [\Psi^\dagger c\vec{\alpha}\Sigma_i\Psi] + \frac{i}{2\hbar}\Psi^\dagger[\hat{H}, \Sigma_i]\Psi \\ &= -\nabla \cdot \vec{J}^{si} + \frac{i}{2\hbar}\Psi^\dagger[\hat{H}, \Sigma_i]\Psi. \end{aligned} \quad (\text{C1})$$

As a result, we can obtain the continuity equation,

$$\frac{d}{dt}\left[\Psi^\dagger\frac{1}{2}\Sigma_i\Psi\right] + \nabla \cdot \vec{J}^{si} = \frac{i}{2\hbar}\Psi^\dagger[\hat{H}, \Sigma_i]\Psi, \quad (\text{C2})$$

and the spin current is defined as  $\vec{J}^{si} = \frac{1}{2}\Psi^\dagger c\vec{\alpha}\Sigma_i\Psi$ . To go further, one can rewrite the spin current density with the NEGF as Eq. (33). In practical calculations, we apply the threefold approximation [19–22] to the current density for maintaining consistency with the calculation of EMTO overlap and Hamiltonian matrices, namely

$$\begin{aligned} J_j^{si}(E, \vec{r}) &= -\frac{ic}{4\pi} \sum_{R\Lambda, R'\Lambda'} G_{R'\Lambda', R\Lambda}^<(E)\Phi_{R\Lambda}^\dagger\alpha_j\Sigma_i\Phi_{R'\Lambda'} \\ &= -\frac{ic}{4\pi} \sum_{R\Lambda, R'\Lambda'} G_{R'\Lambda', R\Lambda}^<(E)[\phi_{R\Lambda}^{a,\dagger}\alpha_j\Sigma_i\phi_{R'\Lambda'}^a\delta_{RR'} - \varphi_{R\Lambda}^{a,\dagger}\alpha_j\Sigma_i\varphi_{R'\Lambda'}^a\delta_{RR'} + \psi_{R\Lambda}^{a,\dagger}\alpha_j\Sigma_i\psi_{R'\Lambda'}^a], \end{aligned} \quad (\text{C3})$$

where  $\phi_{R\Lambda}^a$ ,  $\varphi_{R\Lambda}^a$ , and  $\psi_{R\Lambda}^a$  are the partial wave, free electron solution, and screened spherical wave, respectively. For disordered devices, the disorder-averaged spin-current density can be calculated as

$$\begin{aligned} J_j^{si}(E, \vec{r}) &= -\frac{ic}{4\pi} \left\{ \sum_{R\Lambda, \Lambda'} \sum_Q C_R^Q \mathcal{G}_{R\Lambda', R\Lambda}^{<, Q} [\phi_{R\Lambda}^{a, Q, \dagger} \alpha_j \Sigma_i \phi_{R\Lambda'}^{a, Q} - \varphi_{R\Lambda}^{a, Q, \dagger} \alpha_j \Sigma_i \varphi_{R\Lambda'}^{a, Q} + \psi_{R\Lambda}^{a, Q, \dagger} \alpha_j \Sigma_i \psi_{R\Lambda'}^{a, Q}] \right. \\ &\quad \left. + \sum_{R\Lambda, R'\Lambda'} \sum_{Q, Q'} C_R^Q C_{R'}^{Q'} \mathcal{G}_{R'\Lambda', R\Lambda}^{<, QQ'} \psi_{R\Lambda}^{a, Q, \dagger} \alpha_j \Sigma_i \psi_{R'\Lambda'}^{a, Q'} \right\}. \end{aligned} \quad (\text{C4})$$

In addition, in a similar way, the real-space charge current density for both ordered and disordered devices can be also calculated with FR-EMTO from first principles.

#### APPENDIX D: SPECTRAL FUNCTION FOR DISORDERED SYSTEM

For the disordered system, the averaged spectral functions can be formulated as

$$\bar{A}_B(z, \vec{k}) = -\frac{1}{\pi} \text{Im}[(\mathcal{G}a\dot{S})(z, \vec{k}) - \langle \mathcal{G}a\dot{D} \rangle(z, \vec{k})]_{BB}, \quad (\text{D1})$$

where  $(\mathcal{G}a\dot{S})(z, \vec{k}) = \mathcal{G}(z, \vec{k})a\dot{S}(z, \vec{k})$  and

$$\langle \mathcal{G}a\dot{D} \rangle_{BB}(z, \vec{k}) = \sum_{\vec{T}} \langle \mathcal{G}a\dot{D} \rangle_{B, B+\vec{T}} e^{i\vec{k}\cdot\vec{T}} = \sum_{\vec{T}} \sum_Q C_{B+T}^Q [\mathcal{G} + \mathcal{G}t_{B+T}^Q \mathcal{G}]_{B, B+T} a\dot{D}_{B+T}^Q e^{i\vec{k}\cdot\vec{T}} = \mathcal{G}_{BB}(z, \vec{k}) a((1 + t_B \mathcal{G}_{B,B}) \dot{D}_B), \quad (\text{D2})$$

with  $((1 + t_B \mathcal{G}_{B,B}) \dot{D}_B) = \sum_Q C_B^Q (1 + t_B^Q \mathcal{G}_{B,B}) \dot{D}_B^Q$ . In the spectral function, unphysical poles are removed [18].

- 
- [1] A. Soumyanarayanan, N. Reyren, A. Fert, and C. Panagopoulos, *Nature (London)* **539**, 509 (2016).
- [2] D. Awschalom and N. Samarth, *Physics* **2**, 50 (2009).
- [3] G. H. O. Daalderop, P. J. Kelly, and M. F. H. Schuurmans, *Phys. Rev. B* **41**, 11919 (1990).
- [4] M. T. Johnson, P. J. H. Bloemen, F. J. A. den Broeder, and J. J. de Vries, *Rep. Prog. Phys.* **59**, 1409 (1996).
- [5] L. Liu, C.-F. Pai, Y. Li, H. W. Tseng, D. C. Ralph, and R. A. Buhrman, *Science* **336**, 555 (2012).
- [6] N. Nagaosa, J. Sinova, S. Onoda, A. H. MacDonald, and N. P. Ong, *Rev. Mod. Phys.* **82**, 1539 (2010).
- [7] M. Z. Hasan and C. L. Kane, *Rev. Mod. Phys.* **82**, 3045 (2010).
- [8] X.-L. Qi and S.-C. Zhang, *Rev. Mod. Phys.* **83**, 1057 (2011).
- [9] S. Datta and B. Das, *Appl. Phys. Lett.* **56**, 665 (1990).
- [10] P. Hohenberg and W. Kohn, *Phys. Rev.* **136**, B864 (1964).
- [11] W. Kohn and L. J. Sham, *Phys. Rev.* **140**, A1133 (1965).
- [12] G. Kresse and D. Joubert, *Phys. Rev. B* **59**, 1758 (1999).
- [13] F. Fernández-Seivane, M. A. Oliveira, S. Sanvito, and J. Ferrer, *J. Phys.: Condens. Matter* **18**, 7999 (2006).
- [14] D. Pashov, S. Acharya, W. R. L. Lambrecht, J. Jackson, K. D. Belashchenko, A. Chantis, F. Jamet, and M. van Schilfgaarde, *Comput. Phys. Commun.* **249**, 107065 (2020).
- [15] P. Blaha, K. Schwarz, G. K. H. Madsen, D. Kvasnicka, J. Luitz, R. Laskowski, F. Tran, and L. D. Marks, *WIEN2k: An Augmented Plane Wave plus Local Orbitals Program for Calculating Crystal Properties* (Vienna University of Technology, 2018).
- [16] T. Hühne, C. Zecha, H. Ebert, P. H. Dederichs, and R. Zeller, *Phys. Rev. B* **58**, 10236 (1998).
- [17] H. Ebert, *Phys. Rev. B* **38**, 9390 (1988).
- [18] L. V. Pourovskii, A. V. Ruban, L. Vitos, H. Ebert, B. Johansson, and I. A. Abrikosov, *Phys. Rev. B* **71**, 094415 (2005).
- [19] O. K. Andersen, T. Saha-Dasgupta, R. W. Tank, C. Arcangeli, O. Jepsen, and G. Krier, in *Electronic Structure and Physical Properties of Solids*, edited by H. Dreyssé (Springer, Berlin, 2000), pp. 3–84.
- [20] V. Kumar, O. K. Andersen, and A. Mookerjee, *Lectures on Methods of Electronic Structure Calculations* (World Scientific, Singapore, 1995).
- [21] O. K. Andersen, C. Arcangeli, R. W. Tank, T. Saha-Dasgupta, G. Krier, O. Jepsen, and I. Dasgupta, Third-generation TB-LMTO, *MRS Proc.* **491**, 3 (1997).
- [22] O. K. Andersen and T. Saha-Dasgupta, *Phys. Rev. B* **62**, R16219(R) (2000).
- [23] L. Vitos, H. L. Skriver, B. Johansson, and J. Kollár, *Comput. Mater. Sci.* **18**, 24 (2000).
- [24] L. Vitos, *Phys. Rev. B* **64**, 014107 (2001).
- [25] L. Vitos, *Computational Quantum Mechanics for Materials Engineers: The EMTO Method and Applications* (Springer, London, 2007).
- [26] Q. Zhang, J. Yan, Y. Zhang, and Y. Ke, *Phys. Rev. B* **100**, 075134 (2019).
- [27] I. Turek, V. Drchal, J. Kudrnovský, M. Šob, and P. Weinberger, *Electronic Structure of Disordered Alloys, Surfaces and Interfaces* (Springer, Boston, MA, 1997).
- [28] M. Methfessel, *Phys. Rev. B* **38**, 1537 (1988).
- [29] H. Haug, A.-P. Jauho, and M. Cardona, *Quantum Kinetics in Transport and Optics of Semiconductors*, Vol. 2 (Springer, Berlin, 2008).
- [30] J. Rammer and H. Smith, *Rev. Mod. Phys.* **58**, 323 (1986).
- [31] R. A. Jishi, *Feynman Diagram Techniques in Condensed Matter Physics* (Cambridge University Press, 2013).
- [32] A. K. Field, *Theory of Non-Equilibrium Systems* (Cambridge University Press, 2011).
- [33] G. Stefanucci and R. van Leeuwen, *Nonequilibrium Many-Body Theory of Quantum Systems* (Cambridge University Press, 2013).
- [34] M. Bonitz, *Quantum Kinetic Theory* (Springer, 1998).
- [35] Van-Nam Do, *Adv. Nat. Sci: Nanosci. Nanotechnol.* **5**, 033001 (2014).
- [36] L. V. Keldysh, *Sov. Phys. JETP* **20**, 1018 (1965); Alex Kamenev, *Field Theory of Non-Equilibrium Systems* (Cambridge University Press, 2011).
- [37] R. A. Craig, *J. Math. Phys.* **9**, 605 (1968).
- [38] J. Yan and Y. Ke, *Phys. Rev. B* **94**, 045424 (2016).
- [39] V. Drchal, J. Kudrnovský, and I. Turek, *Comput. Phys. Commun.* **97**, 111 (1996).
- [40] P. Soven, *Phys. Rev.* **156**, 809 (1967).
- [41] D. W. Taylor, *Phys. Rev.* **156**, 1017 (1967).
- [42] L. Vitos, I. A. Abrikosov, and B. Johansson, in *Complex Inorganic Solids: Structural, Stability, and Magnetic Properties of Alloys*, edited by P. E. A. Turchi, A. Gonis, K. Rajan, and A. Meike (Springer, Boston, MA, 2005), pp. 339–352.

- [43] L. Vitos, J.-O. Nilsson, and B. Johansson, *Acta Mater.* **54**, 3821 (2006).
- [44] D. Music, T. Takahashi, L. Vitos, C. Asker, I. A. Abrikosov, and J. M. Schneider, *Appl. Phys. Lett.* **91**, 191904 (2007).
- [45] F. Tian, L. K. Varga, N. Chen, L. Delczeg, and L. Vitos, *Phys. Rev. B* **87**, 075144 (2013).
- [46] F. Tian, L. Delczeg, N. Chen, L. K. Varga, J. Shen, and L. Vitos, *Phys. Rev. B* **88**, 085128 (2013).
- [47] L. Vitos, I. A. Abrikosov, and B. Johansson, *Phys. Rev. Lett.* **87**, 156401 (2001).
- [48] T. A. Maier, M. Jarrell, T. Prushke, and M. Hettler, *Rev. Mod. Phys.* **77**, 1027 (2005).
- [49] C. Zhou and H. Guo, *Phys. Rev. B* **99**, 075414 (2019).
- [50] S. Datta, *Electronic Transport in Mesoscopic Systems* (Cambridge University Press, 1997).
- [51] Y. Ke, K. Xia, and H. Guo, *Phys. Rev. Lett.* **100**, 166805 (2008).
- [52] J. Yan, S. Wang, K. Xia, and Y. Ke, *Phys. Rev. B* **95**, 125428 (2017).
- [53] K. Levin, B. Velický, and H. Ehrenreich, *Phys. Rev. B* **2**, 1771 (1970).
- [54] H. Bauke, S. Ahrens, C. H. Keitel, and R. Grobe, *Phys. Rev. A* **89**, 052101 (2014).
- [55] A. Vernes, B. L. Györfy, and P. Weinberger, *Phys. Rev. B* **76**, 012408 (2007).
- [56] Z. An, F. Q. Liu, Y. Lin, and C. Liu, *Sci. Rep.* **2**, 388 (2012).
- [57] B. K. Nikolic, L. P. Zarbo, and S. Souma, *Phys. Rev. B* **73**, 075303 (2006).
- [58] S. Wang, Y. Xu, and K. Xia, *Phys. Rev. B* **77**, 184430 (2008).
- [59] R. J. H. Wesselink, K. Gupta, Z. Yuan, and Paul J. Kelly, *Phys. Rev. B* **99**, 144409 (2019).
- [60] S. H. Vosko, L. Wilk, and M. Nusair, *Can. J. Phys.* **58**, 1200 (1980).
- [61] See Supplemental Material at <http://link.aps.org/supplemental/10.1103/PhysRevB.102.035405> for more information about the simulation setup and other related results.
- [62] S. LaShell, B. A. McDougall, and E. Jensen, *Phys. Rev. Lett.* **77**, 3419 (1996).
- [63] G. Nicolay, F. Reinert, S. Hüfner, and P. Blaha, *Phys. Rev. B* **65**, 033407 (2001).
- [64] M. Hoesch, M. Muntwiler, V. N. Petrov, M. Hengsberger, L. Patthey, M. Shi, M. Falub, T. Greber, and J. Osterwalder, *Phys. Rev. B* **69**, 241401(R) (2004).
- [65] C. R. Ast, J. Henk, A. Ernst, L. Moreschini, M. C. Falub, D. Pacilé, P. Bruno, K. Kern, and M. Grioni, *Phys. Rev. Lett.* **98**, 186807 (2007).
- [66] G. Bian, X. Wang, T. Miller, and T.-C. Chiang, *Phys. Rev. B* **88**, 085427 (2013).
- [67] K. Xia, M. Zwierzycki, M. Talanana, P. J. Kelly, and G. E. W. Bauer, *Phys. Rev. B* **73**, 064420 (2006).
- [68] K. Dolui and B. K. Nikolic, *Phys. Rev. B* **96**, 220403(R) (2017).
- [69] K. Gupta, R. J. H. Wesselink, R. Liu, Z. Yuan, and Paul J. Kelly, *Phys. Rev. Lett.* **124**, 087702 (2020).
- [70] J. Kudrnovský and V. Drchal, *Phys. Rev. B* **41**, 7515 (1990).